Development of Methodologies for Strain Measurement and Surface Energy Characterization

by

Yougun Han

A thesis
presented to the University of Waterloo
in fulfillment of the
thesis requirement for the degree of
Master of Applied Science
in
Mechanical Engineering

Waterloo, Ontario, Canada, 2011

Author's Declaration

I hereby declare that I am the sole author of this thesis. This is a true copy of the thesis, including any required final revisions, as accepted by my examiners.

I understand that my thesis may be made electronically available to the public.

Abstract

Development of new scientific disciplines such as bioengineering and micro-nano engineering adopting nonconventional materials requests innovative methodologies that can accurately measure the mechanical properties of soft biological materials and characterize surface energy and adhesion properties of them, independent of measurement conditions. One of emerging methods to measure the deformation of materials under stress is digital image correlation (DIC) technique. As a noncontact strain measurement method, DIC has the advantages of prevention of experimental errors caused by the use of contact type sensors and of flexibility in its application to soft materials that are hard to be tested by conventional method. In the first part of the thesis, 2 dimensional and 3 dimensional DIC codes were developed and optimized, and then applied to two critical applications: 1) determining the stress-strain behaviour of polydimethylsiloxane (PDMS) sample, as a model soft material, using the optical images across large deformation region, and 2) detecting the stiffness variation within the gel mimicking the breast tumour using ultrasound images. The results of this study showed the capability of DIC as a strain sensor and suggested its potential as a diagnosing tool for the malignant lesion causing local stiffness variation.

In the characterization of surface energy and adhesion properties of materials, two most common methods are contact angle measurement and JKR-type indentation test. In the second part of the thesis, the experimental set-up for these methods were developed and verified by using the PDMS in static (quasi equilibrium) state. From the dynamic tests, it showed its possible usage in studying adhesion hysteresis with respect to speed. The adhesion hysteresis was observed at high speed condition in both contact angle measurement and JKR-type indentation tests.

Acknowledgements

I would like to express my deepest gratitude to my two supervisors, Dr. HJ Kwon for introducing me to the area of digital image technology and Dr. Boxin Zhao for giving me a chance to know about surface technology. I want to show them my thanks for not only, as mentors in research, their knowledgeable guidance, invaluable insight into research, but also their gracious patience, numerous encouragements for my progress throughout the whole process of my MASc program. I also appreciate their concerns to show me what is important in life. Without their considerate support, it is impossible for me to fulfill the degree. What they did to me is beyond my expectations and will continue to inspire me in my career and life in the future.

My thanks also should go to some of my colleagues. I would like to thank my lab colleague, Allan who shared his idea with me and helped me polish my first manuscript. I could not have achieved it without him. I would like to thank Dr. Dongwoo Kim for planning and designing the ultrasound experiments from the scratch with me. The list would be incomplete if I do not thank my lab mates, Hadi and Kuo, in Nanoadhesion Lab for making cheerful working environment.

Finally, I would like to express my greatest thanks to my family. I express my thanks to my parents, who raised me, inspired me to pursue my own goals, and trust me all the time. I express my thanks to my graceful wife, Rui, for her love, moral support, and getting over all the difficulties with me. I think this achievement is a small return for their constant support.

Table of Contents

List of Figures

List of Tables

Chapter 1
Introduction

The knowledge on materials and the selection of optimum materials are arguably the most essential part in engineering which determines the performances of the resulted system. Numerous material properties such as density, toughness, conductivity, elasticity, viscosity, chemical reactivity and heat transfer should be considered for the successful application. This involves acquiring accurate information of the properties through the measurement methods adopting suitable sensors and instruments. Therefore, instrumentation has always been a critical path into the success of engineering.

Among various material properties, stress-strain behaviour, or simply elastic modulus representing the stress-strain behaviour in a small deformation domain, is one of the most dominant factors in mechanical engineering since different applications require different strain responses to the given stress. Conventionally accurate evaluation of stress-strain behaviour of soft biological materials in large deformation domain has been regarded as extremely difficult, especially in vivo, and the adoption of relatively rough information has been traditionally allowed. However, as new emerging disciplines focusing on bio-related applications such as bioengineering develops, sometimes it is very critical to understand accurate stress-strain behaviour. For example the mechanical properties of human organs such as skin and cartilage would be of interest in designing prosthesis and should be determined precisely [1,2]. Aside from the issue of accuracy, it is also a big challenge to develop a viable solution for in vivo mechanical testing of human organs and tissues, which is more essential in medical practice for diagnosis and surgery planning as well as organ replacement engineering [3,4]. The use of conventional mechanical strain sensors is generally limited in performing mechanical testing for biological applications due to their restriction in space and low accuracy in large deformation. Therefore, precise biomechanical characterization of soft tissues through image analysis has recently attracted much attention [4,5].

Digital image cross correlation (DIC) technique is one of the methods frequently employed for accurate strain measurement of biological tissues [5,6]. This method tracks the movement of multiple points on the digital images of objects by comparing images from different deformed states to a reference image through a certain mathematical algorithm. Using relative displacements of the points, deformation of objects can be estimated. There are various tracking algorithms such as cross-

correlation [7], gradient descent search [8], snake method [9], sum of squared differences [10], and fast normalized cross-correlation (FNCC) algorithm [11].

On the other hand, one of material properties that are receiving more attention ever than before is surface energy and adhesion hysteresis of materials as the technology develops in the micro and nano scale. The effect of contact between two materials becomes more prominent as the length scale decreases and plays a significant role in the performance of the materials and devices when the contacting bodies are sufficiently small. Micro molding would be a good example where the most difficulties of this process arise from demolding because of adhesion forces between the sample and the mold [12]. Also inspired by the hierarchical structures with dimensions ranging from the macroscale to the nanoscale on biological surface and their effects on interaction or adhesion between two surfaces, a large number of researchers have tried to mimic such natural surface structures at ever small scales to solve engineering problems [13]. Gecko foot exhibiting reversible adhesion [14] and lotus leaf performing self-cleaning [13] are well known newly emerging topics.

The two most common methods in studying surface energy and adhesive hysteresis are contact angle measurement and JKR-type indentation test. In contact angle measurement, the angle that forms between liquid and flat solid surface is measured and used to characterize the surface property of the material. In the JKR-type indentation test two solids are brought in direct contact while recording the interacting force, displacement between materials, and the images of contact spot. With these information one can characterize the surface energy of materials using the JKR equation [15].

This thesis comprises two independent studies performed in my Master's study: (i) establishing an accurate strain measurement tool using DIC and its application; (ii) developing contact angle measurement system and JKR-type indentation tester to study surface energy and adhesion behaviour of materials. The first study is described in chapter 2 where the mathematics of DIC algorithm is introduced rigorously. Then the DIC is adopted for two critical applications: 1) determining the stress-strain behaviour of soft material in large deformation region, and 2) detecting the inclusion within the gel mimicking the breast tumour using ultrasound images. The result of first application showed the capability of DIC as a strain sensor that can be used to determine the accurate stress-strain behaviour across large deformation domain which could not be accessed by conventional contact type method. The second application demonstrated the potential of 2D- and 3D- DIC as diagnosing tools for the diseased lesion having different stiffness from the surrounding tissue. Chapter 3 presents the second study in regards to surface energy. The concept of surface energy in relation to the contact

angle and JKR theory is introduced first. Then, two experimental setups developed to measure the contact angle and to perform JKR-type indentation are described. PDMS is used as a model material to validate the contact angle measurement system and JKR-type indentation tester. The surface energies estimated by the methods based on both experimental setups in static or quasi equilibrium states show excellent agreement and are within the range of literature values. A set of dynamic test is also performed and the results suggest its potential as a tool to study adhesion hysteresis.

Chapter 2
Development of a Strain Measurement Method Using DIC and its Application

2.1 Introduction

Digital image cross-correlation (DIC) is an optical method that employs tracking & image recognition techniques for accurate 2D and 3D measurements of changes in images. This is often used to measure deformation, displacement, and strain by tracking multiple points on images of an object or material. The material is usually decorated with speckle patterns; the tracking is achieved by comparing the patterns in the digital images taken before and after deformation. Since it is a non-contact measurement technique, it has advantage of reducing experimental error coming from contacting sensors used by the conventional methods and is very useful when the uses of contact sensors are limited due to certain given experimental conditions [16]. Therefore, its application is rapidly growing in various fields such as biomechanics and metal characterization [17]. For example Thompson et al. employed DIC technique to investigate the local distribution of mechanical strain within regenerating soft tissue sections [5]. Some researchers apply DIC method to study fracture and fatigue behaviours of material [18,19].

Chapter 2 mainly deals with development of in-house developed DIC (2D) and DVC (digital volume cross-correlation, 3D) codes written in Matlab and their applications to two fields: (i) determining the stress-strain behaviour of soft material under large deformation and (ii) diagnosis of malignant tissue in breast. Specifically in section 2.2, the theoretical background on cross correlation and supplementary algorithms (sub-pixel algorithm and data smoothing algorithm) to enhance the accuracy of DIC and DVC performance are discussed rigorously. In section 2.3, DIC is applied to determine the large stress-strain behaviours of soft materials. Optimization of DIC is also fulfilled with respect to referencing method and image frame rate in this section. In the section 2.4, Both DIC and DVC codes were applied to the ultrasound images to obtain full strain field within the phantom which mimics the human breast tissue to validate the possible application of DIC and DVC to diagnosing the cancer in breast.

2.2 Theoretical Background

2.2.1 Fundamental of Cross Correlation

2.2.1.1 Basic concept of cross correlation

Cross-correlation is a technique to quantify the similarity of two sets of signals or data that are acquired with a lagging of time or position. This is also known as a sliding dot product. For continuous functions, f and g, the cross-correlation is defined as:

$$(f \cdot g)(t) \equiv \int_{-\infty}^{+\infty} \overline{f(\tau)} g(t+\tau) d\tau \tag{2-1}$$

where $\overline{f}$ denotes the complex conjugate of f and t is the degree of lagging. Similarly, for discrete functions, with the integer lagging, n, it is defined as:

$$(f \cdot g)(n) \equiv \sum_{m=-\infty}^{+\infty} \overline{f(m)} g(n+m) \tag{2-2}$$

The high cross-correlation value indicates high degree of similarity; therefore, n yielding the highest value can be regarded as the actual lagging between two functions assuming that they have the same form. The concept of the cross-correlation can be understood by considering two real valued functions f and g that differ only by an unknown shift along the x-axis. The formula essentially slides the function g along the x-axis, calculating the integral (or summation) of product at each point. When the functions match, the value of $(f \cdot g)$ is maximized because when positive or negative peaks are aligned, they make a large contribution to integral (or summation).

2.2.1.2 Discrete Fourier transform (DFT)

The discrete Fourier transform (DFT) is one type of discrete transform. It transforms one function into another, which is called the frequency domain representation. It is defined as:

$$F\{x\}_k = X_k = \sum_{n=0}^{N-1} x_n e^{-\frac{2\pi i}{N} kn} \qquad k = 0,\ldots, N-1 \tag{2-3}$$

The inverse discrete Fourier transform (IDFT) can be done by following equation

$$F^{-1}\{X\}_n = x_n = \frac{1}{N}\sum_{k=0}^{N-1} X_k e^{\frac{2\pi i}{N}kn} \qquad n = 0,\ldots,N-1 \tag{2-4}$$

2.2.1.3 Convolution, and Convolution theorem

In mathematics convolution is a mathematical operation of two functions f and g producing a third function that is usually considered as modified version of one of the original functions by the other function called weighting function. It is defined as the integral of the product of the two function after one is reversed and shifted by t.

$$(f * g)(t) \equiv \int_{-\infty}^{+\infty} f(\tau)g(t-\tau)d\tau \tag{2-5}$$

It may be described as the average of the function f at the moment t weighted by the reverse of the function g. Similarly for discrete functions, it is defined as:

$$(f * g)(n) \equiv \sum_{m=-\infty}^{+\infty} f(m)g(n-m) \tag{2-6}$$

And assuming f and g are periodic with period N and if we limit the duration to the interval [0, N-1], the equation can be modified to

$$(f * g)(n) \equiv \sum_{m=0}^{\text{N-1}} f(m)g(n-m) \tag{2-7}$$

We can apply the convolution theorem to this equation. The convolution theorem states that the Fourier transform of a convolution is the pointwise product of Fourier transforms. In this case it is expressed as:

$$F\{\sum_{m=0}^{\text{N-1}} x(m)y(n-m)\}_k = F\{x\}_k \cdot F\{y\}_k \qquad k = 0,\ldots,N-1 \tag{2-8}$$

Proof.

$$
\begin{aligned}
F^{-1}\{F\{x\}\cdot F\{y\}\}_n &= \frac{1}{N}\sum_{k=0}^{N-1} X_k \cdot Y_k \cdot e^{\frac{2\pi i}{N}kn} \\
&= \frac{1}{N}\sum_{k=0}^{N-1}\Big(\sum_{m=0}^{N-1} x_m e^{-\frac{2\pi i}{N}km}\Big)\cdot\Big(\sum_{l=0}^{N-1} y_l e^{-\frac{2\pi i}{N}kl}\Big)\cdot e^{\frac{2\pi i}{N}kn} \\
&= \sum_{m=0}^{N-1} x_m \frac{1}{N}\sum_{k=0}^{N-1}\Big(\sum_{l=0}^{N-1} y_l e^{-\frac{2\pi i}{N}kl}\Big)\cdot e^{\frac{2\pi i}{N}k(n-m)} \qquad n=0,\ldots,N-1 \\
&= \sum_{m=0}^{N-1} x_m \frac{1}{N}\sum_{k=0}^{N-1} Y_k \cdot e^{\frac{2\pi i}{N}k(n-m)} \\
&= \sum_{m=0}^{N-1} x_m y_{n-m} = \sum_{m=0}^{N-1} x(m)y(n-m)
\end{aligned}
$$

Note that x and y were used here instead of f and g to avoid any confusion in using F for the symbol of Fourier transform operator and Fourier transform of the function, f .

2.2.1.4 Similarity between convolution and cross-correlation

According to the definition, it can be found that cross-correlation of $f(t)$ and $g(t)$ is equivalent to the convolution of $f(t)$ and $g(-t)$. Therefore, in the same manner it can be shown that:

$$
F\{\sum_{m=0}^{N-1} x(m)y(n+m)\}_k = \overline{F\{x\}_k}\cdot F\{y\}_k \qquad k=0,\ldots,N-1 \tag{2-9}
$$

Using this relationship, the computational load significantly can be reduced by Fast Fourier Transforms (FFT) which is referred to efficient algorithm to compute the discrete Fourier transform and its inverse. There are many distinct FFT algorithm, but in this thesis they are not discussed.

2.2.1.5 Normalized cross correlation and Fast normalized cross correlation

The cross correlation equation can be modified by subtracting the average value from each function before performing cross correlation. For discrete real functions f of size N and g of size N or bigger, it can be expressed as:

$$
\sum_{m=0}^{N-1}(f(m)-f_{ave})(g(n+m)-g_{ave}) \tag{2-10}
$$

Note that since we are dealing with real value, complex conjugate symbol is not used here. Digital image is a matrix of pixels, and for 8-bit grey image each pixel is expressed in terms of numeric between 0 and 255. The tone gradually changes from black to white as the value increases from 0 to 255. When the functions f and g are cross correlated by Eq. (2-2) the contributions from the pixels with a high grey value are maximized; however, those from the pixels with low grey values are ignored. Eq. (2-10) makes the minimum values negative peaks and take full advantage of the contribution of them while keeping the maximum values as positive peak and their contribution. It also produces negative contribution when two opposite values overlap. Therefore, the resulting correlation values have a better contrast in expressing similarity.

The accuracy of cross-correlation can be further improved by normalizing Eq. (2-10) as:

$$\frac{\sum_{m=0}^{N-1}(f(m)-f_{ave})(g(n+m)-g_{ave,n})}{[\{\sum_{m=0}^{N-1}(f(m)-f_{ave})^2\}\{\sum_{m=0}^{N-1}(g(n+m)-g_{ave,n})^2\}]^{0.5}} \tag{2-11}$$

This is called the normalized cross correlation (NCC) and yields a value of 1 when two data sets are exactly matched and close to 0 when no match is made. Note that in real application g is not periodic and its size is usually bigger than the size of f. Due to the non-periodicity of g and size differences between f and g, computational problems arise. Looking into the numerator which is the same as Eq.(2-10) and the second half of the denominator of Eq. (2-11), respectively, we have,

$$\begin{aligned}\sum_{m=0}^{N-1}(f(m)-f_{ave})(g(n+m)-g_{ave,n}) &= \sum_{m=0}^{N-1} f(m)g(n+m) - Ng_{ave,n}f_{ave} \\ &= \sum_{m=0}^{N-1} f(m)g(n+m) - f_{ave}\sum_{m=0}^{N-1} g(n+m)\end{aligned} \tag{2-12}$$

$$\begin{aligned}\sum_{m=0}^{N-1}(g(n+m)-g_{ave,n})^2 &= \sum_{m=0}^{N-1}\{g(n+m)^2 - 2g(n+m)g_{ave,n} + {g_{ave,n}}^2\} \\ &= \sum_{m=0}^{N-1}\{g(n+m)^2\} - g_{ave,n}\sum_{m=0}^{N-1} g(n+m) \\ &= \sum_{m=0}^{N-1}\{g(n+m)^2\} - \frac{1}{N}\{\sum_{m=0}^{N-1} g(n+m)\}^2\end{aligned} \tag{2-13}$$

When the sizes of f and g are different, we cannot apply convolution theorem and FFT to the first term of Eq. (2-12), $\sum_{m=0}^{N-1} f(m)g(n+m)$ resulting in huge computation load. Nevertheless, this can be easily solved by padding zeros to f and increasing its size up to that of g. However, the terms, $\sum_{m=0}^{N-1} g(n+m)$ and $\sum_{m=0}^{N-1}\{g(n+m)^2\}$ are still problematic regarding the computational load as the number of n increases since one has to calculate the local sum of g and g^2 for each n. This problem can be relieved by adopting the sum table suggested by Louis [11]. Sum table is the pre-calculated look-up table over the whole region of function g, and is referred to each time local sum is calculated. In this case we can make two sum tables:

$$S_1(l) = \sum_{k=0}^{l} g(k) \qquad l = 0,1,2...,L-1 \tag{2-14}$$

$$S_2(l) = \sum_{k=0}^{l} \{g(k)\}^2 \qquad l = 0,1,2...,L-1 \tag{2-15}$$

where L is the size of function g. Using these pre-calculated sums, S_1 and S_2 along the l, One can determine the local sums of g and g^2 following scheme:

$$\sum_{m=0}^{N-1} g(n+m) = \sum_{k=0}^{n+N-1} g(k) - \sum_{k=0}^{n-1} g(k) = S_1(n+N-1) - S_1(n-1) \tag{2-16}$$

$$\sum_{m=0}^{N-1} \{g(n+m)\}^2 = \sum_{k=0}^{n+N-1} \{g(k)\}^2 - \sum_{k=0}^{n-1} \{g(k)\}^2 = S_2(n+N-1) - S_2(n-1) \tag{2-17}$$

NCC adopting the sum-table method in computation is called Fast Normalized Cross Correlation (FNCC). In FNCC, it requires large computational load to make sum-table, but once sum table is completed, it needs little computation to find the local sum. Comparing to NCC which calculates local sum for every n, FNCC can save huge computational resource and time.

2.2.1.6 Multidimensional expansion and its application to images processing (DIC and DVC)

The concepts of DFT, convolution, cross-correlation, NCC, and FNCC can be expanded to multidimensional function or dataset. For digital-image-processing, 2D and 3D images are usually expressed positive two-dimensional and three-dimensional matrix of pixels, respectively. Applying the above algorithms one can track points of interesting by finding the maximum cross-correlation value effectively while sliding latter images over the original or previous image with high efficiency. Based on this, DIC (Digital Image Correlation) and DVC (Digital Volume Correlation) algorithms have been developed for 2D images with 2D matrix data sets and for 3D images composed of 2D image stacks, respectively, using Matlab.

2.2.2 Sub-Pixel Algorithm

Due to the intrinsic nature of discontinuities of digital images composed of pixels, the accuracy of cross-correlation is limited to the size of a pixel and the estimated displacement fields necessarily contain sub-pixel scale errors. To solve this problem, the sub-pixel algorithm based on the quadratic interpolation is additionally implemented. Sub-pixel precision is achieved by fitting a 2nd order polynomial to the maximum correlated point and its surrounding points and finding the local extremum of the polynomial. If the extremum occurs inside the region enclosed by the surrounding points, its position can be considered to be the position of the actual correlated point while the maximum correlated point from the correlation is considered to be real correlated point when it falls outside of the region.

In case of 2D image, assume f is the 2nd order polynomial fitted to the maximum correlated point and the 8 points surrounding it and then

$$\begin{bmatrix} u_{-1,-1} & u_{0.-1} & u_{1,-1} \\ u_{-1,0} & u_{0,0} & u_{1,0} \\ u_{-1,1} & u_{0,1} & u_{1,1} \end{bmatrix} \cong \begin{bmatrix} f(-1,-1) & f(0,-1) & f(1,-1) \\ f(-1,0) & f(0,0) & f(1,0) \\ f(-1,1) & f(0,1) & f(1,1) \end{bmatrix} \tag{2-18}$$

where $f(x,y) = A + Bx + Cy + Dxy + Ex^2 + Fy^2$

This can be expressed in a following matrix form

$$u \cong \phi X \quad \text{where} \quad u = \begin{bmatrix} u_{-1,-1} \\ u_{-1,0} \\ u_{-1,1} \\ u_{0,-1} \\ u_{0,0} \\ u_{0,1} \\ u_{1,-1} \\ u_{1,0} \\ u_{1,1} \end{bmatrix}, \quad \phi = \begin{bmatrix} 1 & -1 & -1 & 1 & 1 & 1 \\ 1 & -1 & 0 & 0 & 1 & 0 \\ 1 & -1 & 1 & -1 & 1 & 1 \\ 1 & 0 & -1 & 0 & 0 & 1 \\ 1 & 0 & 0 & 0 & 0 & 0 \\ 1 & 0 & 1 & 0 & 0 & 1 \\ 1 & 1 & -1 & -1 & 1 & 1 \\ 1 & 1 & 0 & 0 & 1 & 0 \\ 1 & 1 & 1 & 1 & 1 & 1 \end{bmatrix} \quad X = \begin{bmatrix} A \\ B \\ C \\ D \\ E \\ F \end{bmatrix} \tag{2-19}$$

The least square solution, X of this form, i.e., ($\|u - \phi X\|$ is as small as possible) can be found through matrix calculation.

$$X = (\phi^T \phi)^{-1} \phi^T u \tag{2-20}$$

Once the approximate f is found, the coordinates of the extremum are obtained through partial derivatives such as

$$\begin{aligned} \frac{\partial f}{\partial x} &= B + Dy_{extremum} + 2Ex_{extremum} = 0 \\ \frac{\partial f}{\partial y} &= C + Dx_{extremum} + 2Fy_{extremum} = 0 \end{aligned} \tag{2-21}$$

Finally the real correlated position is determined depending on where the point, $(x_{extremum}, y_{extremum})$ falls.

2.2.3 Data Smoothing

Even though smoothing algorithm is implanted, it is almost impossible to eliminate the errors. Since displacement gradient is used in calculating strains based on infinitesimal strain theory, strains are very sensitive to the displacement errors when the distances between the grid points are small. Tracking multiple points to generate strain field usually involves highly dense grid arrays, and rough strain field is frequently generated even from a reasonably smooth displacement data set. To resolve this problem we adopted a smoothing algorithm for uniformly constructed dataset [20]. It is worth noting that image data can be considered equally spaced data set. Smoothing reduces small-scale

experimental noise or error while keeping the most important imprints of a dataset by eliminating random error e_i from the original data y_i.

$$y_i = \hat{y}_i + e_i \tag{2-22}$$

where $\hat{y}_i$ is an unknown smooth function or smoothed data which is the goal of the smoothing process. This would be a suitable method to smoothen coarse strain field image. The employed approach to smoothing is the penalized least square regression [21] that minimizes a criterion function F while balances the fidelity to the data using the following equation:

$$\min\{F(\hat{y})\} = \min\{\sum_{i=1}^{n} (\hat{y}_i - y_i)^2 + sP(\hat{y})\} \tag{2-23}$$

where the first term in right-hand side is the residual sum of squares (RSS), s is a real smoothing parameter, that controls the degree of smoothing, and $P(\hat{y})$ is roughness of smoothed data which can be expressed by using a second-order divided difference [22] as

$$P(\hat{y}) = \left\| D\hat{y} \right\|^2 \tag{2-24}$$

where $\| \ \|$ denotes the Euclidean norm and D is a tri-diagonal square matrix, which for the equally spaced data is given.

$$D = \begin{pmatrix} -1 & 1 & & & \\ 1 & -2 & 1 & & \\ & \ddots & \ddots & \ddots & \\ & & 1 & -2 & 1 \\ & & & 1 & -1 \end{pmatrix} \tag{2-25}$$

Minimizing $F(\hat{y})$ in Eq. (2-23) using Eq. (2-24) gives following linear system that allows the determination of smoothed data

$$\hat{y} = (I_n + sD^T D)^{-1} y \tag{2-26}$$

where I_n and D^T are the n by n identity matrix and the transpose of D, respectively. At this point it is important to use an appropriate smoothing parameter to avoid over- or under- smoothing as much

as possible. Such a correct value can be estimated by the method of generalized cross validation(GCV) introduced by Wahba [21]. Assuming that one wants to solve the smoothing linear system

$$\hat{y} = H(s)y \tag{2-27}$$

where H is the so-called hat matrix (here, $H(s) = (I_n + sD^T D)^{-1}$), the GCV method picks the parameter S that minimizes the GCV score given by

$$GCV(s) \equiv \frac{\sum_{i=1}^{n} (\hat{y}_i - y_i)^2 / n}{(1 - Tr(H)/n)^2} \tag{2-28}$$

where Tr denotes the matrix trace, which can be simply reduced to

$$Tr(H) = \sum_{i=1}^{n} \frac{1}{1 + s\lambda_i^2} \tag{2-29}$$

where $(\lambda_i^2)_{i=1,2,...,n}$ are the eigenvalues of $D^T D$. The GCV score thus reduces to

$$GCV(s) \equiv \frac{n\sum_{i=1}^{n} (\hat{y}_i - y_i)^2}{(n - \sum_{i=1}^{n} \frac{1}{1 + s\lambda_i^2})^2} \tag{2-30}$$

By finding the S value that minimizes the GCV score yielded by Eq. (2-30) makes the smoothing algorithm fully automated. However, because the components of $\hat{y}$ appear in the expression of the GCV score, $\hat{y}$ has to be calculated at each step of the minimization process resulting in huge computational load. Nonetheless in our case this can be avoided since the data set is equally spaced.

An eigendecomposition of the tri-diagonal square matrix D for the equally spaced yields

$$D = U\Lambda U^{-1} \tag{2-31}$$

where Λ is the diagonal matrix containing the eigenvalues of D defined by Yueh [23]:

$$\Lambda = diag(\lambda_1, ..., \lambda_n) \text{ with } \lambda_i = -2 + 2\cos((i-1)\pi / n) \tag{2-32}$$

and U is a unitary matrix (i.e. $U^{-1} = U^T$ and $UU^T = I_n$), in which U^T and U are n-by-n type-2 discrete cosine transform (DCT) and inverse discrete cosine transform matrices (IDCT), respectively [24]. Therefore, we can rewrite Eq. (2-26)

$$\hat{y} = U(I_n + s\Lambda^2)^{-1}U^T y \equiv U\Gamma U^T y = IDCT(\Gamma DCT(y)) \tag{2-33}$$

where the components of the diagonal matrix Γ are given by

$$\Gamma_{i,i} = [1 + s(2 - 2\cos((i-1)\pi / n))^2]^{-1} and \Gamma_{i,i} = 0 \qquad if \quad i \neq j \tag{2-34}$$

Moreover, using Eq.(2-33). the residual sum of squares (RSS) can be written as

$$\begin{aligned} \sum_{i=1}^{n} (\hat{y}_i - y_i)^2 &= \left\| \hat{y} - y \right\|^2 \\ &= \left\| ((I_n + s\Lambda^2)^{-1} - I_n) DCT(y) \right\|^2 \\ &= \sum_{i=1}^{n} (\frac{1}{1 + s\lambda_i^2} - 1)^2 DCT_i^2(y) \end{aligned} \tag{2-35}$$

where DCT_i refers to the i th component of the discrete cosine transform. Note unitary matrix preserves length. Substituting Eq. (2--34) into Eq. (2-30) gives

$$GCV(s) \equiv \frac{n\sum_{i=1}^{n} (\frac{1}{1+s\lambda_i^2} - 1)^2 DCT_i^2(y)}{(n - \sum_{i=1}^{n} \frac{1}{1+s\lambda_i^2})^2} \tag{2-36}$$

The computation of the GCV score from this equation is straightforward and does not require any matrix operation and manipulation, which makes the automated smoothing very fast. Once S value is determined, smoothed function, $\hat{y}$ can be obtained by Eq. (2-26).

2.3 The Application of Digital Image Techniques to Determine the Large Stress-Strain Behaviours of Soft Materials

2.3.1 Introduction

Soft materials such as elastomers, hydrogels and biological tissues have much more complex behaviours and are less understood than pure solids and liquids, but play increasingly important roles in biomedical engineering and micro to nano scale technologies [25-29]. For instance, polyacrylamide chemical gels are employed as the substrate in cell mechanics studies [30], while silicone rubbers are used as implantable cosmetic reconstructive materials due to their biocompatibility and tissue-like mechanical properties [1]. One of the applications in which reliable mechanical properties might be critical is the injection of bio-polymer based hydrogels into the highly stressed environment of the heart wall to ward off end stage heart failure[31].

Accurate strain measurement in a large deformation region is particularly challenging for soft materials. Standard tensile test schemes [32,33] use dumbbell shaped specimens. These schemes minimize the effect of grip region tri-axial stress state observed in stress-strain results generated with straight (strip) specimens [34] , but typically necessitate the use of contact type sensors to isolate gauge section response from the overall deformation. Unfortunately the stiffness of contact type sensors prevents their applications to soft materials. Under the assumption that deformation primarily takes place in the gauge section, gauge response is frequently approximated by overall elongation [35-37]. However, at high strains deformation outside the gauge section becomes considerable which makes this approach inaccurate [37]. Recognizing this problem, some researchers introduced a constant correction factor determined by manual measurement or FEM (finite element method) simulation, to convert the overall strain to the gauge section strain [37]. Use of a constant correction factor is valid at small strains or when a constant ratio is maintained between strains inside and outside of the gauge section; however, the nonlinear stress-strain relationships common in soft materials result in strain ratios that are functions of elongation. Another confounding factor when gauge length elongation is not directly measured is the slip between the sample and the grips [38,39]. Self tightening grips may not respond properly to specimens below certain stiffness while fixed grips cannot respond to the thickness reduction induced by an axial deformation.

To directly measure the gauge section strains, non-contact sensors such as video and laser extensometers are used. Analyzing video data from a tensile test using digital image cross correlation

(DIC) [16,40,41] is one of the most popular methods since it can measure the strain field in a large domain. This method tracks the movement of multiple points on the sample surface by comparing images from different deformed states to a reference image. Using relative displacements of the points the complete strain field can be estimated with sub-pixel accuracy [7,16].

Two types of referencing schemes are possible. Under fixed referencing an image from the undeformed state is used as a reference image [42]. This scheme is not susceptible to accumulated error as all comparisons are made back to the undeformed state; however, when specimen deformation becomes severe the difference between images may prevent accurate results from being obtained. Dynamic referencing overcomes this difficulty by using the previous deformed state as a reference but at the cost of allowing the potential for accumulated error. Many studies, e.g. [40,43] , have used DIC to characterize mechanical properties of materials; however, few studies published in the open literature have considered the effect of referencing scheme on the performance of DIC. This may be partly because the commercial codes utilized do not allow dynamic referencing [44].

This study used polydemethylsiloxane (PDMS) elastomer as a model soft material due to its purely elastic behaviour and the ease of fabrication. There have been a few studies applying DIC to PDMS under several deformation modes, (Berfield et. al. [40]: under tensile, Nunes [41]: under shear); however, these studies were limited to the small deformation regime. This study investigated the performance of various testing methods including DIC by applying them to large deformation of PDMS, and validated the results with virtual test procedure. We expect that the testing methods proposed in this study can be applied to characterize the large deformation behaviour of other soft materials.

2.3.2 Experimental

2.3.2.1 Specimen preparation

PDMS was prepared from a two-component kit (Sylgard Elastomer 184, Dow Corning Corporation, Midland, MI). The base and cross-linker were mixed at a ratio of 10:1 for 10 minutes, degassed in a desiccator for 15 minutes and cast into a Teflon mold. Samples were cured in an oven at 90 °C for 90 minutes under an unconfined condition, i.e. the mold was not capped during curing. Dumbbell and strip specimens with geometries shown in Fig. 2.1(a) were produced.

The DIC method requires proper patterning on the specimen surface. Random speckle patterns were generated by spraying opaque black paint (Createx) with an airbrush (Eclipse HP-CS, Iwata). The airbrush has a 0.35 mm nozzle diameter, allowing for an excellent paint diffusion and high resolution of tiny paint droplets (speckles) as shown in Fig. 2.1(b). It was verified in preliminary tests that the surface patterning did not affect the mechanical properties of the specimen.

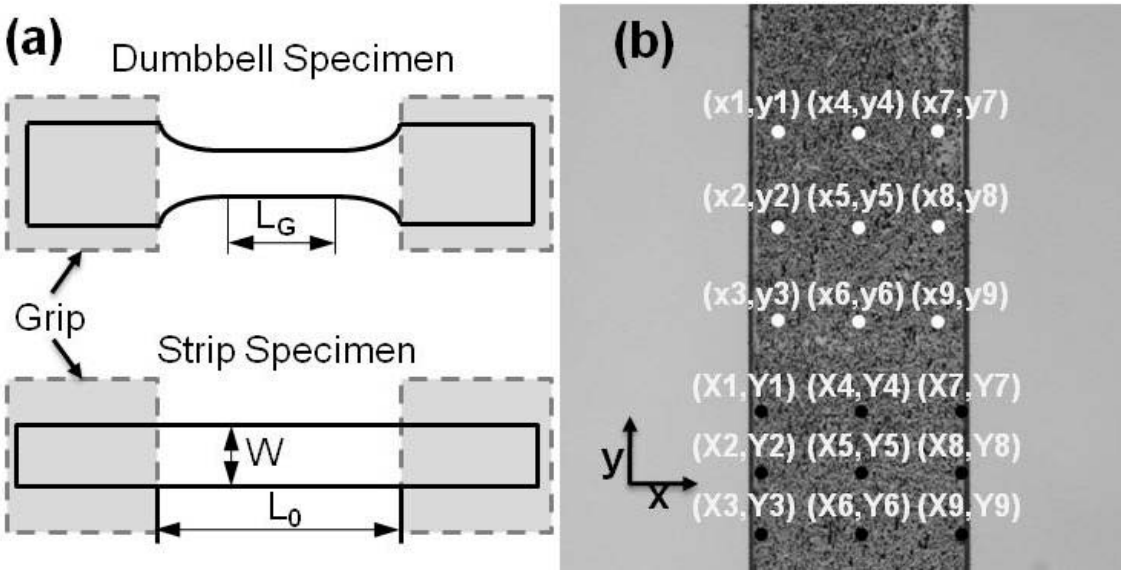

Figure 2.1. (a) The geometries of the specimens, and (b) the gauge section image under tension on which grid points for DIC analysis are indicated: undeformed (Xi, Yi) and deformed (xi, yi) positions of grid points.

2.3.2.2 Test setup

Tensile tests were performed using a TA material testing machine (TA.xt Plus, Stable Micro Systems, New Jersey) with a 5 kgf load cell. During the tests, force, displacement, and time were recorded by the computer while specimen images were captured by a high resolution CCD camera (1028x1008 pixels, STC-CL202A, SENTECH) through a camera link (NI PCIe-1427, National Instrument). The CCD camera with a 25 mm manual focus iris lens was placed 70 mm away from the specimen, resulting in a spatial resolution of 56.06 pixels/mm. Mechanical testing and image capture were synchronized and controlled by a custom developed LabVIEW code (V8.5, National Instrument).

2.3.2.3 Tensile tests

Both dumbell and strip type specimens were used for tensile tests. To determine the influence of strip specimen aspect ratio, the length to width ratio was varied between 1 and 15, (L_0/W in Fig. 2.1(a)).

Cyclic tensile tests, consisting of five loading-unloading cycles, were used to examine the error accumulation and grip slippage. In each cycle, tensile loading was applied until the engineering stress reached 2 MPa. Unloading continued until the cross-head returned to its initial position. Between cycles any residual compressive stress or change in specimen shape was noted and released by moving the cross-head until the load became zero. Ultimate tensile tests were also conducted to determine the overall stress-strain curve and failure point. A constant crosshead speed of 12mm/min was used for all tests (loading and unloading).

2.3.2.4 Stress / Strain calculation

Engineering stress, σ_E and strain, ε_E were calculated using the following relationships,

$$\sigma_E = \frac{F}{A_0} \tag{2-37}$$

$$\varepsilon_E = \frac{\Delta L}{L_0} \tag{2-38}$$

where F is the force measured by the load cell, A_0 initial cross-sectional area, L_0 original length and ΔL elongation. Strains were estimated in two ways. In conventional testing schemes (CS) using overall elongation [33-35], crosshead displacement was measured to be used as ΔL in Eq. (2-38). In the tests using dumbbell specimens, L_G in Fig. 2.1(a) was taken as L_0, while initial distance between the grips was regarded as L_0 for strip specimens. In DIC method (DIC), nine rectangular grid points were chosen in the middle of the gauge section following ASTM standard [45] to be tracked by the FNCC algorithm, as shown in Fig. 2.1(b). The engineering strain was calculated by averaging the strains of those points as:

$$\varepsilon_E = \frac{\Delta L}{L_0} = \frac{(y_3 + y_6 + y_9 - y_1 - y_4 - y_7) - (Y_3 + Y_6 + Y_9 - Y_1 - Y_4 - Y_7)}{(Y_3 + Y_6 + Y_9 - Y_1 - Y_4 - Y_7)} \tag{2-39}$$

where Y_i are the y-directional coordinates of grid points on the undeformed image, and y_i y-coordinates of the same grid points on the deformed images tracked by DIC. True strains in x- and y-axis directions were also calculated from the displacements of grid points as

$$(\varepsilon_x)_T = \ln\frac{L_f}{L_0} = \ln\frac{(x_3 + x_6 + x_9 - x_1 - x_4 - x_7)}{(X_3 + X_6 + X_9 - X_1 - X_4 - X_7)} \tag{2-40}$$

$$(\varepsilon_y)_T = \ln\frac{L_f}{L_0} = \ln\frac{(y_3 + y_6 + y_9 - y_1 - y_4 - y_7)}{(Y_3 + Y_6 + Y_9 - Y_1 - Y_4 - Y_7)} \tag{2-41}$$

Note that displacement rate (i.e. infinitesimal strains, $\varepsilon_{ij} = 0.5(\partial u_i / \partial x_j + \partial u_j / \partial x_i)$) are commonly adopted for strains in DIC applications; however, this is not valid in large deformations.

By assuming a plane stress condition in the gauge section, Poisson's ratio ν was determined by using Eqs. 2-40 and 2-41:

$$\nu = -\frac{(\varepsilon_x)_T}{(\varepsilon_y)_T} \tag{2-42}$$

2.3.2.5 DIC optimization

The effect of referencing scheme on DIC performance was investigated by applying fixed and dynamic referencing schemes to a simple tensile test. Images were taken during the test using the dumbbell specimen elongated up to 70 %. The images were analyzed using both schemes.

The effect of frame rate using dynamic referencing was examined by a simple translation test. In this test a speckle patterned glass plate clamped in the TA testing machine was moved vertically upward at a speed of 20 μm/s while pictures were taken at 5 frames per second. Different frame rates of 2.5, 1.67, 1.25, 1, 0.5, 0.25, 0.125, and 0.066 fps were achieved by skipping images at fixed intervals in the DIC analysis to simulate a range of frame rates. The corresponding displacements of the reference image were 0.112, 0.224, 0.449, 0.676, 0.897, 1.121, 2.24, 4.49, 8.97, and 17.94 pixels per frame. Error was determined by comparing the average displacement calculated for nine points to the known displacement.

2.3.2.6 Virtual tensile test

To estimate the accuracies of the stress-strain curves determined by various testing methods, tensile tests were simulated using FEM. In this simulation, load-displacement curves were produced by 3-D FEM model (ABAQUS 6.5 Standard) of dumbbell specimen consisting of 1024 20-node quadratic brick elements, employing each stress-strain curve as a material property. Considering the geometrical symmetry of the specimens, only half quarters of the specimens were modeled. The empirical constitutive equation obtained through curve-fitting to experimental stress-strain curve was coded into the FEM model using UMAT that is a user-defined module in ABAQUS for material properties.

Since the empirical constitutive equation is highly nonlinear, the stress-strain relationship based on linear elasticity (Hooke's law) cannot be used for UMAT. Also other nonlinear elastic stress-strain functions provided by ABAQUS such as hyperelasticity cannot be matched with the stress-strain curve. Therefore, new stress-strain relations based on the proposed constitutive equation should be defined. For this, experimentally determined uniaxial stress-strain curve was regarded as effective stress-strain curve, and assumed to be the stress function for the deformation. For monotonically increasing loading, nonlinear elastic deformation and plastic deformation cannot be discerned; therefore, the incremental deformation theory of plasticity [46] could be invoked as:

$$\bar{\sigma} = f(\bar{\varepsilon}) \tag{2-43}$$

$$d\varepsilon_x = \frac{d\bar{\varepsilon}}{d\bar{\sigma}}\left[d\sigma_x - \nu(d\sigma_y + d\sigma_z)\right] \tag{2-44}$$

$$d\varepsilon_y = \frac{d\bar{\varepsilon}}{d\bar{\sigma}}\left[d\sigma_y - \nu(d\sigma_z + d\sigma_x)\right] \tag{2-45}$$

$$d\varepsilon_z = \frac{d\bar{\varepsilon}}{d\bar{\sigma}}\left[d\sigma_z - \nu(d\sigma_x + d\sigma_y)\right] \tag{2-46}$$

$$d\gamma_{xy} = 2(1+\nu)\frac{d\bar{\varepsilon}}{d\bar{\sigma}}d\tau_{xy} \tag{2-47}$$

$$d\gamma_{yz} = 2(1+\nu)\frac{d\bar{\varepsilon}}{d\bar{\sigma}}d\tau_{yz} \tag{2-48}$$

$$d\gamma_{zx} = 2(1+\nu)\frac{d\bar{\varepsilon}}{d\bar{\sigma}}d\tau_{zx} \tag{2-49}$$

where $\bar{\sigma} = f(\bar{\varepsilon})$ is the newly proposed constitutive equation where $\bar{\sigma}$ and $\bar{\varepsilon}$ are the effective stress and effective strain, respectively. $d\varepsilon_{ij}$ and $d\gamma_{ij}$ are the strain increment tensors at each step.

2.3.3 Results and Discussion

2.3.3.1 DIC optimization

2.3.3.1.1 Referencing optimization

In Fig. 2 the abilities of fixed and dynamic referencing to track the progress of specimen deformation are qualitatively compared. When the deformation is small, both schemes yield almost the same results; however, as the deformation becomes significant, fixed referencing cannot follow the movements of the grid points (Fig. 2.2(a)), while the dynamic referencing consistently demonstrated excellent tracking capability (Fig. 2.2(b)).

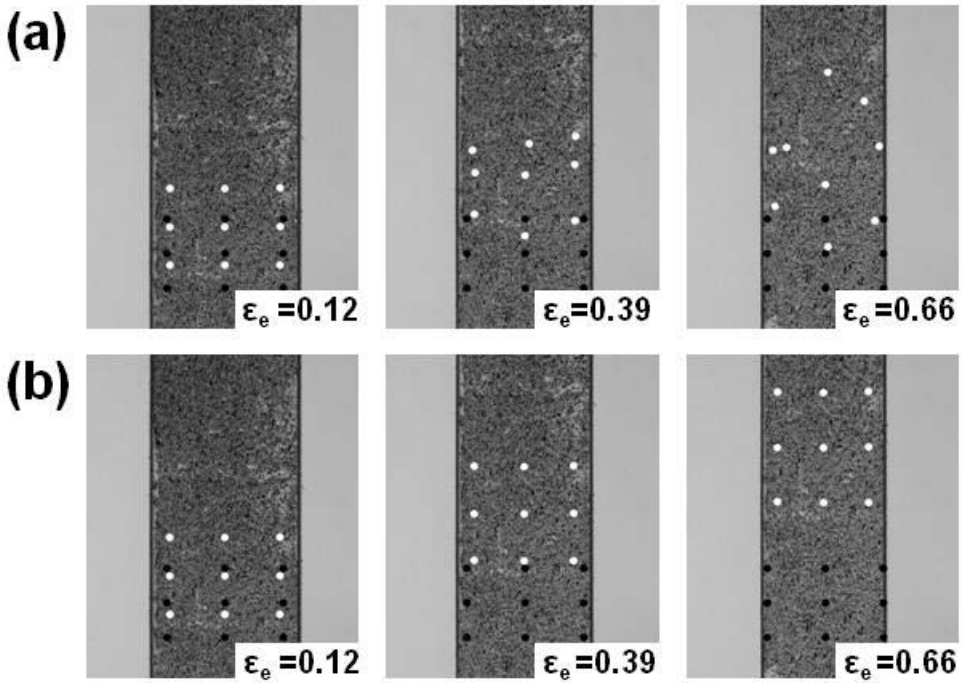

Figure 2.2. Qualitative comparison of image tracking abilities: (a) fixed referencing, and (b) dynamic referencing. The engineering strains were measured under dynamic referencing.

For a quantitative comparison between the two referencing schemes the average of NCC values, degree of matching for the 9 grid points in Fig. 2.2(a) and 2.2(b) are plotted in Fig. 2.3. While the NCC value for dynamic referencing is very consistent in the vicinity of 0.9 out of a possible 1.0; a steady decline and increasing scatter for the fixed referencing scheme indicate a decreasing ability to identify the new location of a point with increasing deformation. When the strain exceeds 0.13 the NCC value drops below the threshold of 0.5 indicating that the result is unreliable.

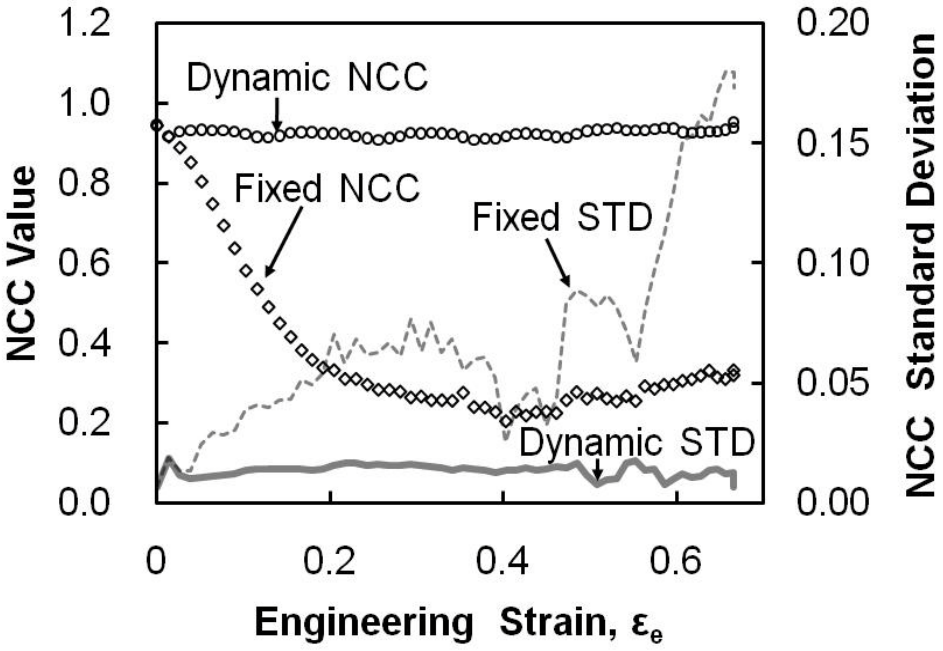

Figure 2.3. Plots of average normalized correlation coefficients (NCC) and their standard deviations (STD) under fixed and dynamic referencing.

2.3.3.1.2 Frame rate optimization

The effect of frame rate on DIC performance adopting dynamic referencing is presented in Fig. 2.4, using the pixel movement per frame as the abscissa, and as the ordinate the estimated average displacement of 9 grid points for the known displacement of 9.95mm. It can be seen that even though the real displacement falls within a standard deviation for all tested frame rates, acceptable accuracy is only obtained when the movement per frame is greater than one pixel. Even with the sub-pixel algorithm using quadratic interpolation, movement less than one pixel cannot be accurately estimated. It is also observed that the increase of displacement per frame over one pixel do not have any

significant influence on accuracy, with the error in each case being in the order of 1%. This should be caused by the discontinuous nature of DIC data. If the frame rate is high so that multiple estimated movements of less than one pixel are added together under dynamic referencing, these errors are accumulated to lead the incorrect results. Conversely, error in estimating movements greater than one pixel appears to be truly random allowing it to cancel itself out as multiple results are summed together for the final displacement. Note that the error due to sub-pixel movement is not accumulated in fixed referencing.

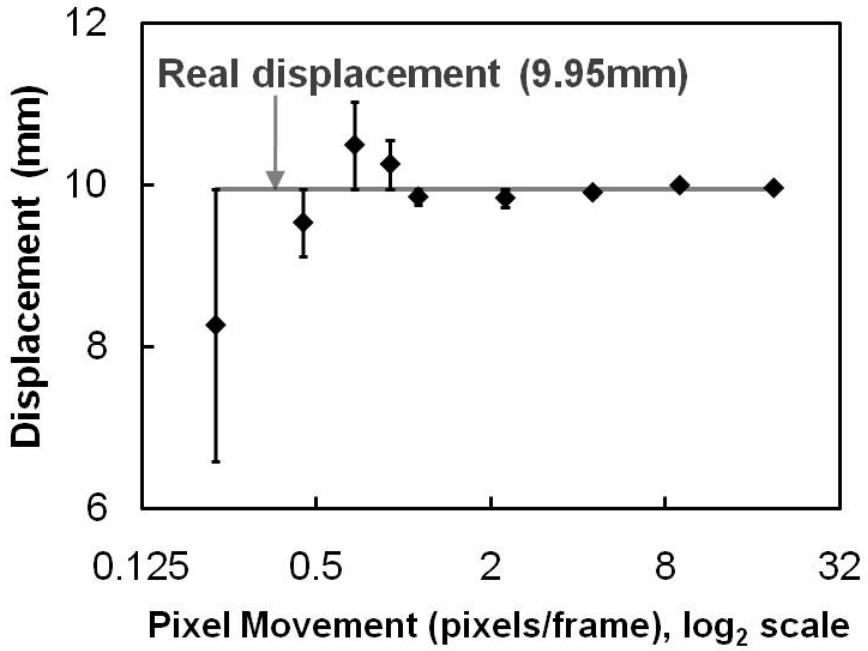

Figure 2.4. The dependence of DIC performance on image frame rate. 9.95 mm translation was measured by DIC using the images taken at different frame rates under dynamic referencing.

Based on the above results the dynamic referencing scheme with frame rate adjusted to a minimum displacement of one pixel per frame between two consecutive images was employed for the primary analysis.

2.3.3.2 Cyclic tensile tests on dumbbell specimen

Fig. 2.5 shows engineering stress-engineering strain curves from 5 cycles of loading-unloading tensile tests performed on a dumbbell specimen, evaluated by conventional scheme (CS) and DIC method. Loading and unloading branches are indicated by upward and downward arrows, respectively. It is

notable that the stress-strain curve in the first cycle evaluated by CS (CS-1 in Fig. 2.5) deviates from other CS curves (CS-2~5), and a large hysteresis loop was formed by the loading and unloading branches. This is attributed to the significant amount of irreversible slip between the sample and the grips. Lateral thinning of the sample associated with axial strain induces a certain amount of slip of the sample out of the grips depending on the degree of deformation. Usually this kind of slip is nearly unavoidable and the result would erroneously show a larger strain than actually occurs in the material or (and) fallacious permanent strain [38,39]; however, this irreversible slip occurred only once in the first cycle as the specimen settled in the grips.

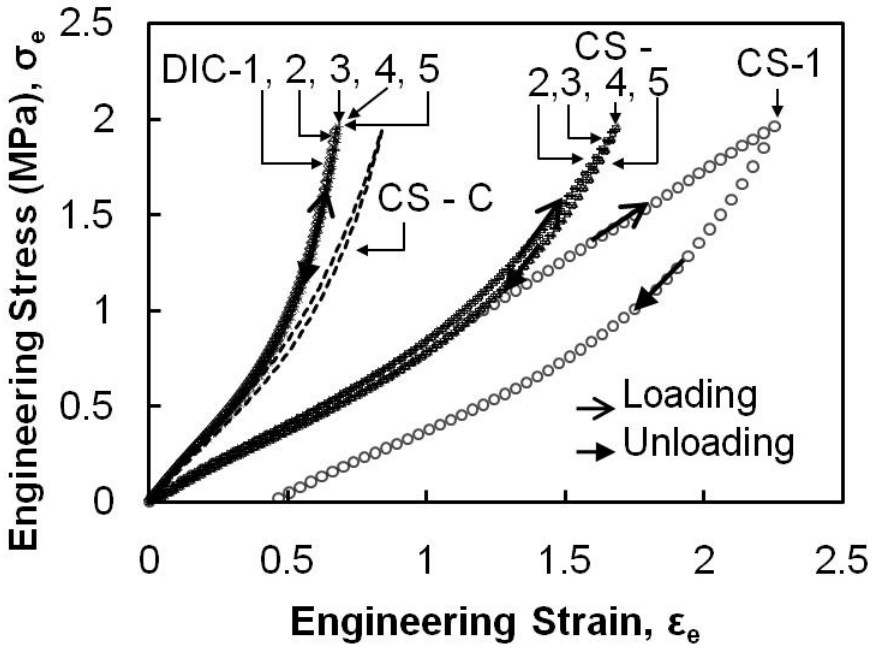

Figure 2.5. Engineering stress-strain curves from cyclic tensile tests on dumbbell specimens measured by conventional scheme (CS), corrected conventional scheme (CS-C), and DIC.

The high degree of consistency observed in loading / unloading curves after the first cycle, CS-2 to 5 in Fig. 2.5, suggests no irreversible process occurred during these tests. A small amount of hysteresis was observed which might be attributable to material viscoelastisty or some other dissipative process.

Little or no hysteresis was observed in DIC results which are all in good agreement with one another and fall onto a single curve (DIC-1~5). This suggests that DIC method is highly robust to slip and can yield consistent result irrespective of slip.

It is interesting to note that the DIC stress-strain curves are significantly different from those given by CS-2~5, with the stress level in DIC curves more than twice of that in CS at the same strain. It is known that the CS overestimates the strain due to the deformation outside the gauge section [36,37]. Schneider et al. [37] multiplied the measured strain by a correction factor of m = 0.49~0.50 to convert the overall strain to gauge section strain. Following this scheme CS-C in Fig. 2.5 was generated. While it is much closer to the DIC curve, differences still exist in magnitude of stress and the level of hysteresis loop. Adjusting correction factor cannot resolve the difference.

The difference was further investigated to estimate the reliabilities of CS and DIC based measurements.

2.3.3.3 Hysteresis analysis

Hysteresis loop in cyclic stress-strain curve is one of the properties typifying visco-elastic materials. Other visco-elastic properties include stress relaxation and creep. To verify the visco-elastic properties of tested PDMS, specimens were loaded at constant strain and at constant stress, respectively, for 24 hours to investigate the stress relaxation and creep behaviours. The test results (not included in this paper) show that stress relaxation or creep did not occur in the tested PDMS. This is consistent with the previous reports suggesting that fully cured PDMS is purely elastic at room temperature [47,48]. Therefore, we concluded that the tested PDMS should not have visco-elastic properties and the hysteresis loop presented by CS-C curve must have come from some other cause.

Careful examination of the gripping area revealed that a small portion of the specimen slipped out from the grip region under tensile loading but retracted to its original position when it was unloaded. This slip resulted in a changing effective gauge length during CS based measurements. The frictional forces between the grip surfaces and sample at the slip region oppose movement resulting in differing effective gauge lengths at the same load in the loading and unloading branches, which should have caused the hysteresis loop. The overlapping of the CS-2~5 curves indicated that this type of slip was reversible and no sign of slip left after unloading, which makes the detection extremely difficult. On the contrary, DIC measurements guarantee a constant gauge length and are made only in the middle of the gauge section where the uniaxial stress assumption is most valid and so avoid this difficulty.

The fact that this slip in the grips can introduce hysteresis must be considered in studies dedicated to viscoelastic properties, particularly in the large deformation/non-linear region.

2.3.3.4 Cyclic tensile tests on strip specimen

CS based grip settling behaviour was similar to dumbbell specimen, i.e. existence of irreversible and reversible slips. Because of these slips, the stress strain curve was estimated from the loading portion of the subsequent cycles in Fig. 2.6. Comparing the stress-strain curves for subsequent cycles, a trend of increasing apparent stiffness with increasing L_0/W is observed. This trend becomes less prominent as L_0/W ratio becomes higher, and the curves superimpose at L_0/W ratios above about 15. The variation of stress-strain curve with L_0/W can be explained by the variation of stress state within the strip specimen. Because of the constraint by gripping, the stress state in the vicinity of end grip is close to triaxial, which changes gradually to uniaxial as the distance from the end grip increases. The size of the triaxial region in the influence of the end grip is independent of the strip length. Therefore, the increase of L_0/W causes the decrease of the ratio of the material volume affected by triaxial stress state, and the measured stress-strain curve approaches the one from purely uniaxial stress state. Since the stress-strain curves in Fig. 2.6 converge to the curve for L_0/W =15, it should be very close to the uniaxial stress-strain curve. The insert of Fig. 2.6 shows both of loading and unloading portions for SS-1 and 15 indicating that the observed hysteresis is inversely proportional to L_0/W. This bears out our previous speculation that it is grip induced rather than inherent to the material. DIC results are again highly consistent for all L_0/W ratios tested (DIC-SS in Fig. 2.6) and in almost perfect agreement with the dumbbell results (DIC-Dumbbell). Therefore, it can be stated that optimized DIC can yield the stress-strain curve independent of specimen geometry. The similarity between the DIC curve and the one for L_0/W=15 suggests that SS with L_0/W>=15 may be adequate if extreme accuracy is not necessary.

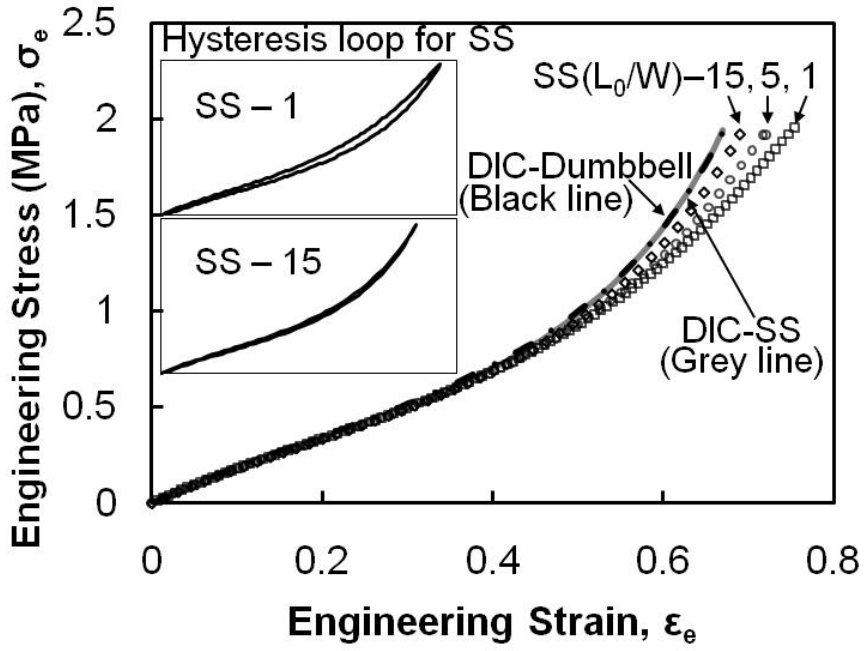

Figure 2.6. Engineering stress-strain curves from the cyclic tensile tests on strip specimens.

2.3.3.5 Ultimate tensile tests

The results from ultimate tensile tests were analyzed by DIC and Schneider et al's corrected crosshead displacement scheme [37], CS-C. In Fig. 2.7 they are compared to the results obtained by Khanafer and coworkers [49] for the same material using crosshead displacement. Note that Ref. [49] proposed a 3rd order polynomial equation for the curve fitting. The curve from strip specimen for $L_0/W=15$ were converted into true stress-true strain curve using Eq. (2-41) and also plotted (SS) in Fig. 2.7. Poisson's ratio was required for this conversion of engineering stress into true stress. From axial and transverse true strains measured by DIC and Eq. (2-42), Poisson's ratio was determined to be 0.5±0.03 which is consistent with the common belief that fully cross-linked PDMS is be incompressible [50,51]. From this result, Poisson's ratio was assumed to be 0.5.

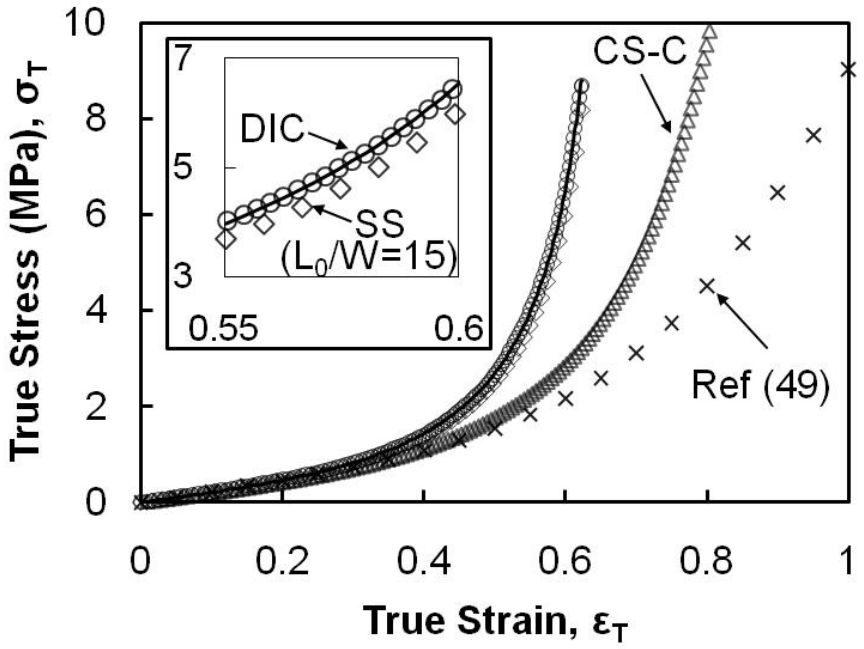

Figure 2.7. True stress-strain curves from DIC, SS, CS-C, and Ref. (49).

All four curves overlap in small strain region, showing almost linear increasing trend up to around 0.2. They start rising exponentially beyond that strain, indicating that strain-hardening becomes more significant with the progress of deformation. Different hardening behaviours are demonstrated by different curves, with DIC being the most significant followed by SS, CS-C, and the curve from Ref. [49]. DIC and SS curves look very similar; however, the magnified view in the insert shows that there is a difference.

Note that the severe strain hardening behaviours in DIC or SS curves in Fig. 2.7 cannot be fitted by the 3rd order polynomial proposed by Ref. [49]. We had also attempted to use common constitutive models such as rubber elasticity [52], Mooney and Rivlin [53], BST equation[54], G'Sell and Jonas [55] to describe the observed non-linear behaviours. However, none of them provided good agreements except the BST equation, which has a very complex form with 4 fitting parameters. The resulting fitting parameters in BST equation do not have any intrinsic meaning, and it is difficult to make a link to the deformation mechanism [56].

Based on the observed strong strain-hardening behaviour with an almost vertical asymptote at large strain, we proposed the following form of constitutive equation to describe the stress-strain behaviour across large strain region:

$$\sigma_T = E\left[\varepsilon_T + \frac{(\varepsilon_T)^A}{B-\varepsilon_T}\right] \tag{2-50}$$

where E is elastic modulus; A and B are two fitting constants related to the strain-hardening behaviour. Eq. (2-50) has enough flexibility to fit all four curves in Fig. 2.7 almost perfectly using the fitting constants in Table 2.1 that are evaluated by least square fitting method. The first term in Eq. (2-50) dominates true stress when strain is small, while the importance of second term increases with the increase of strain. Note that Eq. (2-50) has the vertical asymptote at $\varepsilon_T = B$, which implies that the stiffness approaches infinity as the strain is getting close to B. The specimen could not be deformed up to asymptotic strain, as the specimen failed before gauge section strain reached that strain because of the stress concentration at the round corner between gauge and nongauge sections.

Table 2-1. Constants in Eq. (14) for the stress-strain curves from DIC, SS, CS-C, and Ref. (49)

	E (MPa)	A	B
DIC	1.980	2.537	0.701
SS (L_0/W=15)	1.922	2.610	0.704
CS-C	2.197	2.603	0.958
Ref. (49)	2.379	2.537	1.345

2.3.3.6 Virtual tensile test using FEM

Fig. 2.8 shows the load-displacement curves from the FEM simulations and the experiment. The FEM simulation adopting the DIC stress-strain curve shows an excellent agreement with the experimental data (circle), while other simulation results deviate from the experimental data in the similar manner as their stress-strain curves deviate from DIC stress-strain curve. The deviations are noticeable in large strain region; however, the magnified view in small strain region (insert in Fig. 2.8) also illustrates that simulation result using DIC curve is in much better agreement with the experimental data than any others. The errors between the load-displacement curves from the experiment and simulations are quantified by using the R-squared value for the load-displacement curves, with R-squared value being 1 when two curves are perfectly matched. Table 2.2 shows that the R-squared value for the simulation curve adopting DIC stress-strain curve is almost 1, while those from other simulations are getting lower than 1 in the order of SS, CS-C and literature. These results indicate that

stress-strain curves evaluated by DIC method best represents the real stress-strain behaviour and should be very close to actual material property.

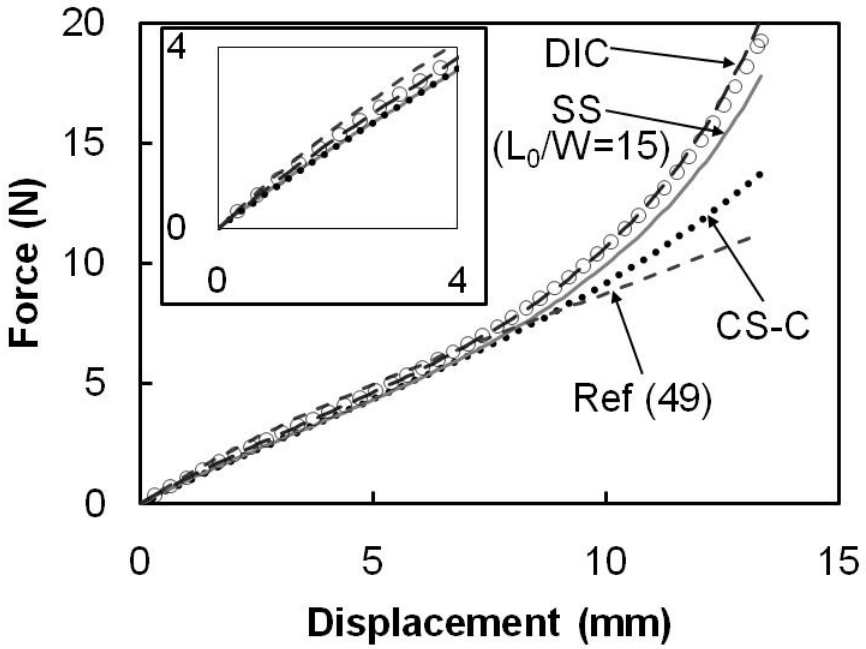

Figure 2.8. Load-displacement curves from experiment (○) and the FEM simulations adopting constitutive equations for DIC, SS, CS-S, and Ref. (49).

Table 2-2. R-squared values for the load-displacement curves from experiment and the simulations adopting different stress-strain curves

Method	DIC	SS (L_0/W=15)	CS-C	Ref. (49)
R^2	0.9987	0.9799	0.7882	0.3776

2.3.3.7 Asymptotic strain-hardening

The constitutive equation in Eq. (2-50) suggests strong strain-hardening behaviour caused by both the power law relation in the numerator and the asymptote in the denominator. The power-law equation in the numerator induces comparable degree of strain-hardening as rubber elasticity theory in small strain region. Rubber elasticity assumes that the free energy change in deformation is due to the restraints placed on configurational rearrangement, and is considered to be totally entropic in origin [56]. However, this theory is only applicable to small strains, since the considerable change in the

end-to-end distance of the network chains would distort the Gaussian distribution of the statistical elements.

As the strain increases and approaches the asymptotic strain ε_T = 0.701, different type of hardening takes place in a much more significant manner. This strain hardening may be induced by strain crystallization [57,58], alignment of covalent-bonded polymer chains in the stretching direction. When PDMS is moderately deformed under tension, polymer chains are disentangled and re-oriented to be aligned along the loading direction, which can be represented by the power law relation in the numerator in Eq. (2-50) or rubber elasticity model. As the strain approaches asymptotic strain, polymer chains are pulled taut that the forces are mostly carried by covalently bonded polymer chains, and the measured stiffness approaches that of polymer chains. Since the covalent bonding is extremely stiff compared to other types of bondings and stiffening mechanisms, the stress-strain curve takes the form of vertical asymptote as presented in Fig. 2.7.

2.3.4 Conclusion

This study showed that the selection of reference image has a major influence on the accuracy of DIC results and the adoption of dynamic referencing with a suitable frame rate in DIC analysis can yield much better results than fixed referencing. Optimized DIC method was applied to a large deformation of soft materials. PDMS was used as model soft material and its stress-strain relationship across a large deformation region was evaluated. The comparative study of the stress-strain curves obtained from the conventional tensile test schemes and DIC method suggested that the DIC technique is robust to the slip between the sample and the grips while the accuracy of conventional test scheme is highly affected. The true stress-strain relationship of PDMS in tension evaluated by DIC showed a significant strain-hardening behaviour, with a vertical asymptote at strain ε_T = 0.701. Based on this behaviour a new type of constitutive equation was proposed to account for the significant strain-hardening in large strain region, and showed excellent agreement with the experimental stress-strain curves. FEM simulation adopting the constitutive equation successfully produced the load-displacement curve showing excellent agreement with experimental data. This suggests that the stress-strain curves determined by the DIC can be used to represent the actual stress-strain behaviour of PDMS. Poisson's ratio of PDMS was also verified to be 0.5 in tension. The optimized DIC technique and analysis method used here may be able to be applied to the studies of other elastomers, gels and biological tissues.

2.4 Diagnosis of Breast Tumour Using 2D and 3D Ultrasound Images

2.4.1 Introduction

Cancer is the top leading cause of death in North America [59,60]. Among the various cancers, breast cancer is the most common malignancy in women and the second most common cause of cancer-related death [60]. In the past several years, the early detection and treatment of breast carcinoma has received increased attention [61]. Prior to the advent of diagnostic imaging, the detection involved palpation. Malignant tumours feel harder than benign ones which is related to the pathological changes in their elastic and visco-elastic mechanical properties [62]. While palpation is simple, it is just a qualitative assessment and can only be applied to superficial organs. The results are also open to user interpretation [63]. Recently mammography has been widely used for the early detection of breast cancer [64]. Even though it has contributed to the reduction of mortality, high false positive causing additional testing or biopsy, and the possibility of overdiagnosis and overtreatment arguably outweigh the benefits [65]. The addition of MRI (magnetic resonance imaging) to the screening algorithm adds considerable cost over $50,000 per cancer [64]. Ultrasound imaging is relatively affordable and accessible; thus it has been given interests as a modality to supplement or replace mammography, especially for the women with dense breasts [66]. However, in many cases, the lesion may not possess sufficient echo graphic properties and therefore, it is hard to detect using B mode ultrasound image (sonogram).

Recently, elastography has received an attention as a method to estimate the elastic properties of biological tissues [62,67-70]. Elastograms are obtained by estimating the strain variations using the time-gradient of ultrasound echo data, obtained before and after a slight compression of the tissue, i.e.

$$e_{11} = \frac{(t_{1b} - t_{1a}) - (t_{2b} - t_{2a})}{t_{1b} - t_{1a}} \tag{2-51}$$

where t_{1a} and t_{1b} are the arrival times of the pre-compression echoes from the proximal and distal windows, respectively; t_{2a} and t_{2b} are the arrival times of the post-compression echoes from the proximal and distal windows, respectively [62]. The resulting strain fields are displayed as an image, where soft areas appear white and hard areas appear black. The mean depth and width of the lesion on the elastogram and sonogram were measured and used as parameter for differentiating benign and

malignant lesions [66,71,72]. Since elastogram images can be displayed almost simultaneously with sonogram images, it is a very useful practice in diagnosing disease. However, it is hard to be used as a tool for material characterization of tissues, as elastogram is highly degraded in large strain deformations because of the decorrelation due to lateral and elevational deformation [69]. Moreover the direction of loading should be the same as that of ultrasound wave; thus only the axial strain in the loading direction can be estimated. Also the deformation under tension is hard to be investigated. Other drawbacks include the lack of 3D capability.

We applied Digital Image Correlation (DIC) method to 2D sonogram images to characterize the mechanical properties of the phantom mimicking breast tissue. The displacement and the strain fields around the cylindrical inclusion were estimated by DIC implemented with smoothing algorithm. Using the estimated strain field, the stiffness of the inclusion representing carcinoma could be accurately estimated. This study was extended to full 3D analysis of 3D sonogram images using in-house developed Digital Volume Correlation (DVC) algorithm. The 3D shape of the inclusion and the stiffness of the inclusion can be estimated by this analysis.

2.4.2 Experimental

2.4.2.1 Sample Preparation

Soft and hard gels were made with 1% agarose (by weight), 2% glutar aldehide, 5% propanol, 5% and 20% gelatin, respectively, and water (the remaining weight %). Hard and soft gels were used for the inclusion and the outer material, respectively.

Samples preparation procedure was as follows: After water was heated up to 85°C, agarose, gelatin, and propanol were added in order. After 3 min of solution time, glutar-aldehide was added, and was heated for 4 more min. The solution containing 20% gelatin was suck into a 3 ml syringe (inner diameter of 8.6 mm) and kept at room temperature for 48 hours for gelation. Then, the resulting gel was taken out and stored in water to prevent shrinkage. Using the same protocol, the solution with 5% gelatin content was prepared and poured into a long cylindrical mold (diameter of 4 cm and height of 8 cm) in half. When temperature decreased to 35°C, the prepared inclusion containing 20% gelatin was placed on top of the solution and gelled for 5 minutes. Then, the solution was added up to the end of the mold and kept for 48 more hours. This procedure is illustrated in shown in Fig. 2.9. The sample from this mold is referred as the phantom in the rest of the thesis.

Using the same protocol, other cylindrical samples with the diameter and height of 4 cm each (aspect ratio of 1) containing 5% and 20%, respectively, were made to measure the elastic modulus of soft and hard samples.

2.4.2.2 Compression Test

Compression tests were performed using a TA material testing machine (TA.xt Plus, Stable Micro Systems) with a 5 kgf load cell. Each sample was loaded up to the engineering strain of 0.1 at the speed of 10 μm/s. The elastic modulus was determined to be 47±2 kPa for hard sample with 20% gelatin content and 9±1 kPa for soft sample 5% gelatin content.

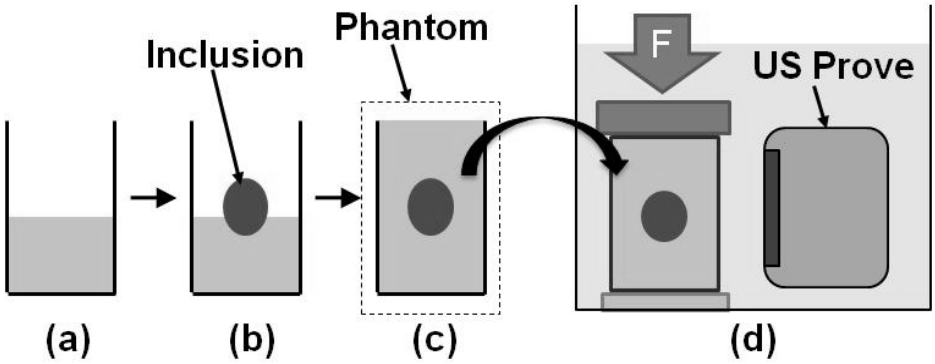

Figure 2.9. The schematics of procedures for making phantom and 2D US test setup: (a) solution containing 5% gelatin was poured into the mold in half. (b) Once the temperature dropped to 35 °C the prepared inclusion containing 20% gelatin was placed on top of it. (c) Then, the solution was poured to fill the mold. (d) In 2D US test, the phantom was uniaxially compressed while the US probe acquired US image of deformed phantom

2.4.2.3 2-Dimensional Test

The phantom was uniaxially compressed to reach 10% nominal strain. At each 1% strain step, US image was recorded using the commercial medical ultrasound image machine (Accuvix XQ, Medison). Note that US probe was placed in the compression direction, was perpendicular to the cylindrical inclusion so that the inclusion was imaged circular, as shown in Fig. 2.9(d). The obtained image has the size of 450 × 435 pixels with space resolution of 82.5μm/pixel. In non-deformed image, multiple points were selected at every 15 pixels in both x and y directions and FNCC algorithm implemented with sub-pixel algorithm was applied to track these points through the deformed images.

Since 10% strain is relatively large, instead of fixed reference scheme (using the non-deformed image as the reference), dynamic referencing scheme (updating and using the previous deformed state as a reference for the processing image) was employed. Based on the acquired relative displacements of points of interests, displacement and strain (gradient of displacement) field were drawn in the direction of compression.

2.4.2.4 3-Dimensional Test

For the 3D test the probe was installed on a motorized linear stage (T-LSM050A, Zaber) in the direction perpendicular to the loading direction, as shown in the Fig. 2.10(a). 500 2D US images were taken by moving the probe stepwise along the height of the sample before and after compression of 1% strain. 3D image stacks were generated by piling up these 2D images as shown in Fig. 2.10(b). Resulting 3D image has a size of 430 × 230 x 500 pixels. Tracking points were selected at every 10 pixels in all the direction from the undeformed 3D image. The modified FNCC algorithm was employed to estimate the displacement of each tracking point. Based on the relative displacements of the tracking points, displacement and strain fields were estimated in the direction of compression.

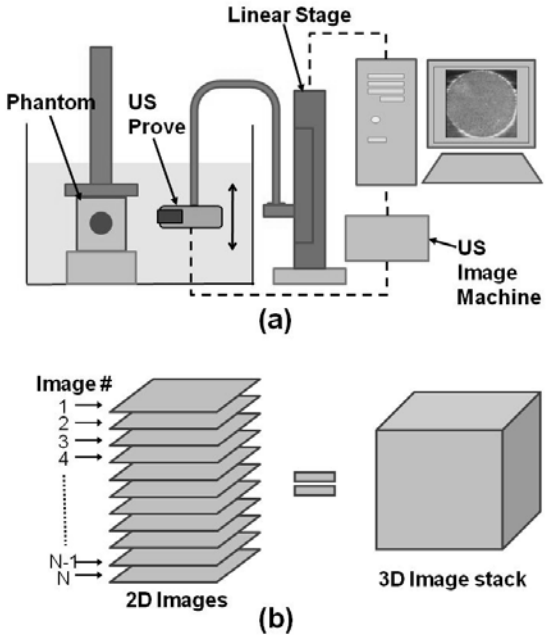

Figure 2.10. The schematic of 3D test. Lateral cross sectional 2D US images are taken moving the position of the probe step by step along the sample. (b) 3D US images are generated by stacking on 2D US images .

2.4.3 Results and Discussion

2D displacement and strain field images estimated by DIC are presented with US B-mode images in Fig. 2.11. B-mode images indicate the hard inclusion has similar echogenecity as the surrounding soft gels and is hard to be detected. The existence of inclusion can be recognized from both displacement and strain field images. However, strain field is very rough and irregular even though displacement field is relatively smooth, because of the intrinsic sensitivity of strain (displacement gradient) to sub-pixel errors. The roughness of strain field does not allow the accurate estimation of the size and relative modulus of the inclusion compared to the outer portion of the phantom.

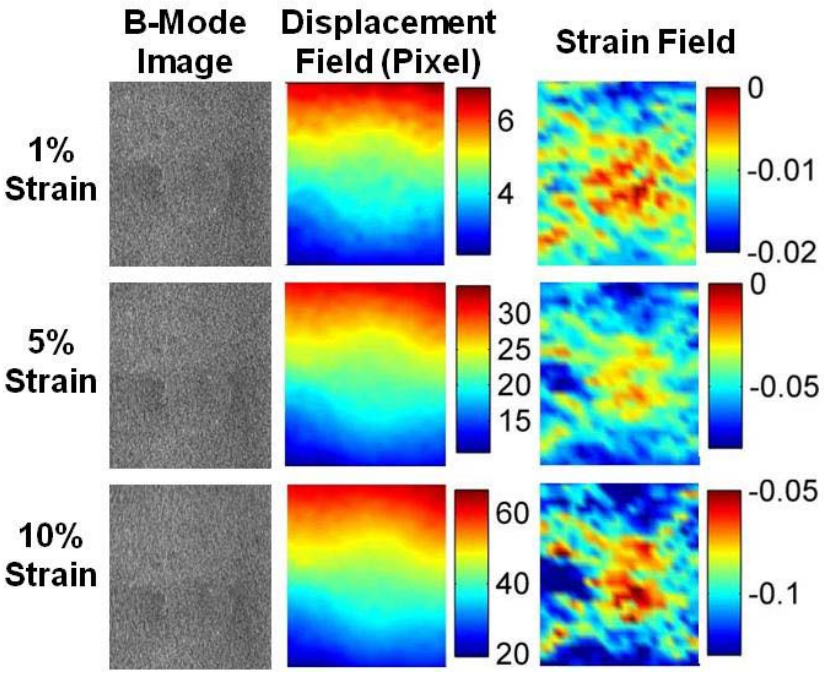

Figure 2.11. B-mode, displacement field, and strain field images of phantom in deformation.

Roughness of strain field can be alleviated by applying smoothing algorithm in three ways: (i) to the strain field, (ii) to the displacement field, and (iii) to the displacement field, and then to the strain field generated from a smoothed displacement field. The results are shown in Fig. 2.12 with the strain field without smoothing in the first column. All three results show smooth strain fields with noticeably low strain region in the center corresponding to the inclusion. By comparing the original shape of the inclusion with the low strain regions in the strain images, combined smoothing in which both displacement and strain were smoothed yielded the most satisfactory result.

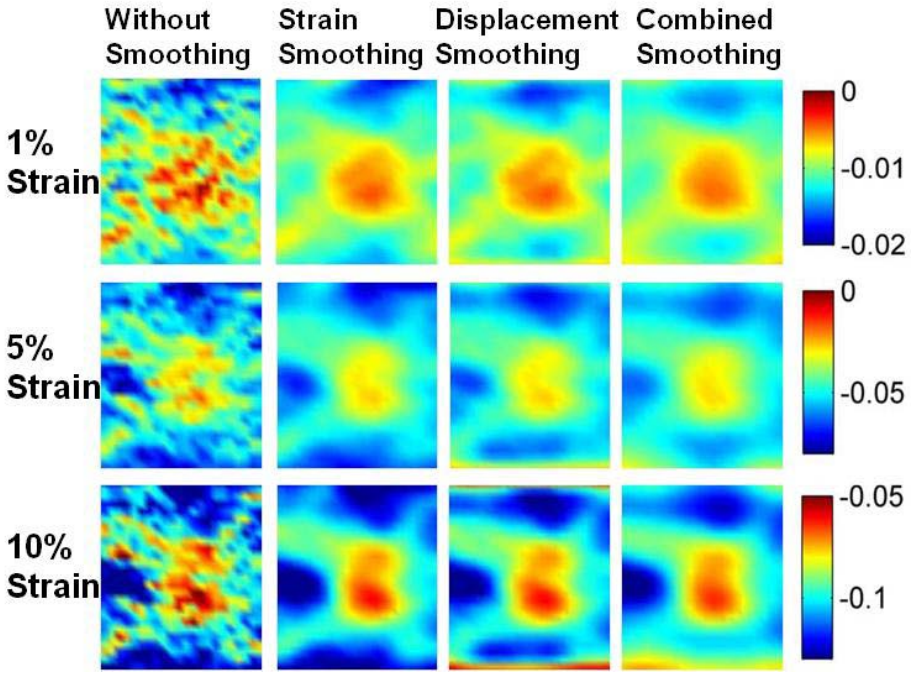

Figure 2.12. The effect of application of smoothing algorithm: smoothing strain only, smoothing displacement only, and smoothing both displacement and strain.

By applying DVC to 3D images of undeformed and deformed sample of 1% strain, displacement and strain fields were produced as shown in Figs 3.13(a) and (b). Close observation on Fig. 3.13(a) reveals that displacement field is slightly distorted in the center region, which may suggest the existence of an inclusion. However, no notable indication of inclusion was found in the strain field in Fig. 3.13(b). By applying the combined smoothing scheme as in 2D, the inclusion could be clearly identified as shown in Fig. 3.13(c). The 3D shape of inclusion was also estimated by the DVC as shown in Fig. 3.13(d).

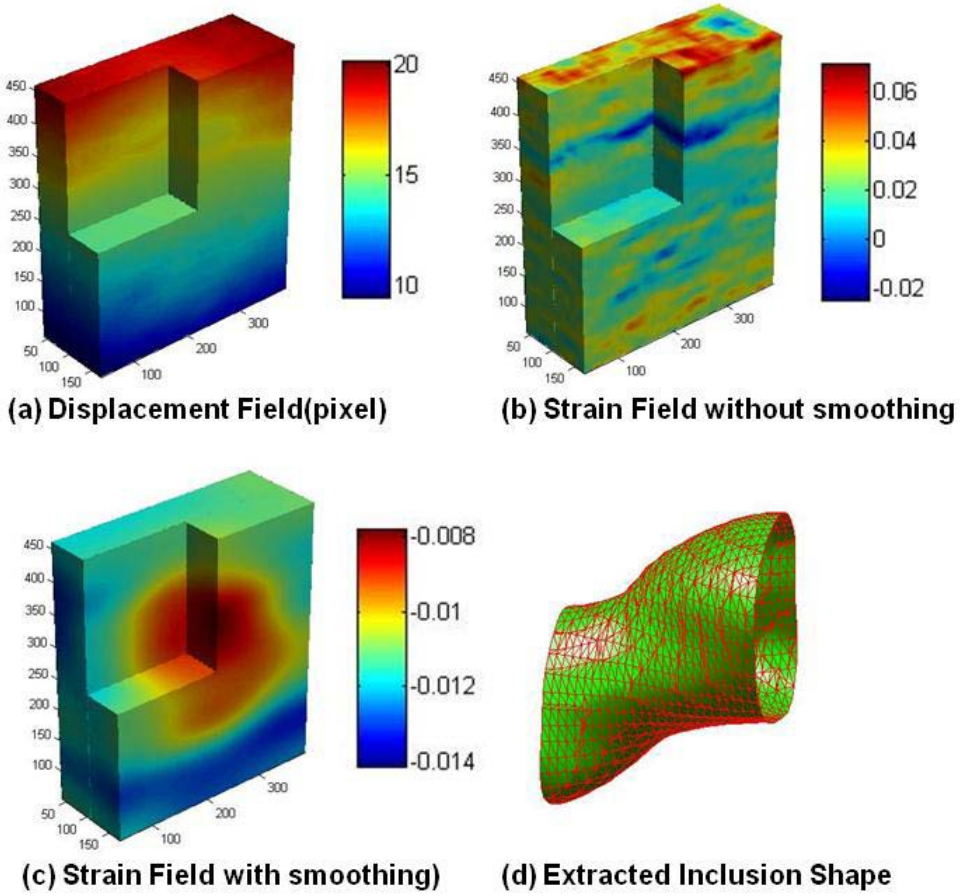

Figure 2.13. (a) 3D displacement field, (b) 3D strain field without smoothing. (c) 3D strain field with smoothing, and (d) extracted inclusion shape.

The smoothed 2D and 3D strain fields, also known as elastogram [69], allowed us to estimate the ratio of elastic modulus of inclusion and outer region. The elastic modulus ratio was determined by the strain ratio based on the assumption that both inclusion and outer region are under uniform stress field and follow the linear stress-strain relationship as:

$$\sigma = E_{inclusion}\varepsilon_{inlusion} = E_{outer}\varepsilon_{outer} \quad \Rightarrow \quad \frac{E_{inlusion}}{E_{outer}} = \frac{\varepsilon_{outer}}{\varepsilon_{inlusion}} \tag{2-52}$$

Because there is smooth transition of strain from outer to inclusion, $\varepsilon_{inlusion}$ and ε_{outer} was determined from the strain values at the center of the inclusion and the remote region from the inclusion, respectively. Diameter of the inclusion was determined by using the 80% of the strain at

the center of the inclusion as a threshold value that distinguishing inclusion and outer material. The results are shown in the table 2-3.

Table 2-3. modulus ratio between inclusion and outer part and estimated diameter of inclusion

		Elastic Modulus Ratio ($E_{inlusion} / E_{outer}$)	Inclusion Diameter (mm)
2D	1% strain	3.14	9.9
	5% strain	2.43	11.1
	10% strain	2.17	9.2
3D (2.5% strain)		2.12	10.9
Actual value		4.8	8.6

The estimated elastic modulus ratio is smaller than the actual ratio, while estimated diameter is slightly larger than the actual value. The difference may be partly caused by the smoothed strain field. Also, the applied stress should not be uniform across the phantom because of the existence of the inclusion.

Usually malignant tumours are harder than benign tissues [69] and therefore, elastogram is often used to detect carcinomas [68,73,74]. However, the conventional elastogram based on time gradient has poor resolution, so that the application has been limited, even though it has the advantage of real time imaging. The 2D DIC based elastogram has better resolution and can detect the size and the relative elastic modulus with reasonable accuracy.

One of the applications of 3D elastogram may be biopsy. When a suspected cyst is found by modalities such as mammogram or MRI, biopsy is frequently conducted to sample fluid or remove clusters of cells. In this practice, the information on the location and the shape of the suspected cyst should be very helpful. 3D elastogram proposed in this study can be used as a guide to perform biopsy.

2.4.4 Conclusion

Digital image correlation algorithm was applied to produce 2D and 3D displacement and strain fields. Strain field can be significantly improved by adopting smoothing algorithm. The ratio of elastic

modulus of inclusion to that of outer material and the diameter of inclusion in phantom were estimated from strain field.

This study shows the potential to apply DIC and DVC algorithms with smoothing function to the in-vivo diagnosis of pathological tissue within the body, and to provide new information that is related to tissue structure and or pathology.

Chapter 3
Development of Apparatuses for Characterizing Surface Energy

3.1 Introduction

As future technological innovations gear toward miniaturizing machines and maximizing performance density, the contact between similar or dissimilar materials has become one of the most critical technical concerns in designing materials both chemically and mechanically. The surface effects (adhesion, surface energy, and associated micro-mechanical properties) play an important role in the performance of the materials and devices at small length scales. For example, in the processes of micro-molding and nano-imprinting, the adhesion and subsequent detachment between the polymer and micro/nano-structured templates are essential steps during the transfer of the micro/nanoscale patterns [75]. Not only the contact between solids, but also the contact between solid and liquid is of great interest and has been studied extensively. The ability of pond skaters to walk on the surface of water has attracted many researchers. In mimicking this ability of pond skaters, the interaction between water and material may be one of the most important factors [13] .

When liquid is in contact with a surface, it forms different shapes depending on the wetting capability of the liquid on the surface. The main parameter that characterizes wetting is the contact angle, which is defined as the angle that forms between the liquid and the surface. Conventionally it is defined that the surface is hydrophilic if the contact angle of water is between 0° and 90° whereas the surface is hydrophobic if the contact angle of water is between 90° and 180°.

Studying the wetting behaviour on the surface of a material is of interest in various applications, including biomimetic materials and biomaterials. Biomimetic is the study of nature, its models, systems, and processes to solve engineering problems. Applying self-cleaning phenomenon known as the “Lotus effect” to self-cleaning windows, windshields, exterior paints for buildings and navigation ships would be examples of biomimetic [13]. Biomaterials are nonviable materials used in a medical device, indented to interact with biological system. In implantation of biomedical devices and prostheses, one has to consider the foreign body reaction to their material and surfaces such as inflammation since these implanted devices would be degraded by the response of the body. Generally it is known that hydrophilic surface prevents the cells from adhering to the surface and thus

from affecting the materials [3, 4]. Therefore, in designing the biomaterial, its hydrophobicity has to be taken into account.

The contact between solids has also been an important issue in various applications in terms of external force, material deformation, and contact area and mainly pioneered by Hertz's early work back in 1886 [78]. The conventional application would be contact between rail wheels and roads. Recently the contact problem at the micro or nano scales starts to gain attention and but cannot be explained by Hertz theory because Hertz theory ignored the surface interaction between the solids. Johnson et al [15] took the surface interaction into account and developed the Johnson-Kendall-Roberts (JKR) theory. The effect of surface interaction is significant at small length scales and therefore, should be considered in the micro and nano technology. The JKR theory based indentation test is becoming standard method to study surface property of materials and their interaction [75,79-81].

This chapter consists of three parts. In section 3.2, the theoretical backgrounds on contact angle and contact mechanics are discussed. The meaning of contact angle is described in terms of thermodynamic concepts. Hertz and JKR theories are rigorously derived, and the way surface energy is related to JKR theory is explained. In section 3.3, custom developed contact angle measurement system and JKR-type indentation tester are introduced. Lastly, section 3.4 presents the study of dynamic contact behaviour of PDMS examined by both contact angle measurement (PDMS-water) and JKR-type indentation test (PDMS-PDMS).

3.2 Theoretical Background

3.2.1 The Contact Angle of a Liquid on a Solid Surface

The following theoretical treatment is based on the reference [82].

3.2.1.1 Interfacial tension

Interfacial tension (or surface energy) is defined to be an additional free energy per unit area caused by the presence of an interface. In thermodynamics, the attraction between a fluid A molecule and a fluid B molecule must be less than the average of that between two A molecules and that between two B molecules to separate fluids A and B and to form the interfacial region as shown in Fig.

3.1. Here the phrase "interfacial region" is used instead of the word "interface" because the transition between two bulk compositions takes place over a finite thickness rather than a two dimensional surface. For convenience, two surfaces SF_A and SF_B can be selected to express the interfacial region. Hence the energy per molecule must be greater in the interfacial region than in the bulk fluids.

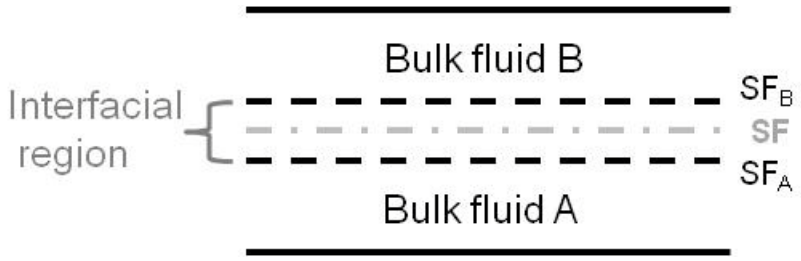

Figure 3.1. Interface between two different bulk fluids

The internal energy, U of this interfacial region differs from the value, $U_A + U_B$ which would be determined by assuming that bulk phases A and B extend unchanged all the way to SF which represents an interface as a mathematical surface with zero thickness. The difference is called the surface excess internal energy, and is assigned to SF (i.e. U^{SF}).

$$U^{SF} = U - U_A - U_B \tag{3-1}$$

Similarly, surface excess values of other thermodynamic properties can be defined. For example, the surface excess number of moles, n_i^{SF} of species i can be defined.

$$n_i^{SF} = n_i - n_{iA} - n_{iB} \tag{3-2}$$

Here n_i is the actual number of moles of i in the region between SF_A and SF_B, n_{iA} is the moles of i that would be present in the region between SF_A and SF if it were occupied by bulk fluid A, and n_{iB} is defined similarly for the region between SF_B and SF.

Now consider the change of surface excess internal energy under equilibrium conditions. If the system in Fig. 3.1 keeps its shape, then its internal energy, U is a function only of its entropy, S and the number of moles of species i, n_i in the system. Therefore, the change of surface excess internal energy can also be expressed as follow:

$$dU^{SF} = TdS^{SF} + \sum_i u_i dn_i^{SF} \tag{3-3}$$

If the reference surface, SF deforms so that the area of SF changes, then

$$dU^{SF} = TdS^{SF} + \sum_i u_i dn_i^{SF} + \gamma dA \tag{3-4}$$

It was mentioned that the energy per molecule must be greater in the interfacial region than in the bulk fluids. Therefore, the energy of interfacial region increases and γ is positive. It should be noted that curvature of SF also change when the surface deforms, but we can expect the effect to be small if the radii of curvature are much larger than the interfacial thickness.

The Helmholtz free energy F for the interfacial region is defined in the usual way.

$$F = U - TS \tag{3-5}$$

We can also think about surface excess Helmholtz free energy F for the interfacial region

$$F^{SF} = U^{SF} - TS^{SF} \tag{3-6}$$

Differentiating Eq. (3-6) and substituting Eq. (3-4) gives

$$dF^{SF} = -S^{SF} dT + \sum_i u_i dn_i^{SF} + \gamma dA \tag{3-7}$$

It is clear from this equation that given the temperature without mass transfer the interfacial tension can be written in terms of the surface excess free energy as

$$\gamma = \left(\frac{\partial F^{SF}}{\partial A}\right)_{T, n_i^{SF}} \tag{3-8}$$

Using Gibbs free energy instead of Helmholtz free energy in the derivation gives the same result under the assumption that pressure and volume of the system are constant.

3.2.1.2 Liquid contact angle on a solid surface

Considering the change in Helmholtz free energy of the total system in the previous section (3.2.1.1), we can write

$$
\begin{aligned}
dF &= dF^{SF} + dF_A + dF_B \\
&= -S^{SF}dT + \sum_i u_i dn_i^{SF} + \gamma dA \\
&\quad - S_A dT + \sum_i u_i dn_{iA} - p_A dV_A \\
&\quad - S_B dT + \sum_i u_i dn_{iB} - p_B dV_B
\end{aligned}
\tag{3-9}
$$

Now let's consider a liquid droplet on a smooth solid surface as shown in Fig. 3.2. There are three interfaces: the solid(S)-liquid(L), the liquid-vapor(V), and the solid-vapor. Thus, there exists three interfacial tensions γ_{SL}, γ_{SV}, and γ_{LV}. The angle that forms between the liquid and the surface is called the contact angle. The relationship between three interfacial tensions and the contact angle can be found in the following thermodynamic consideration.

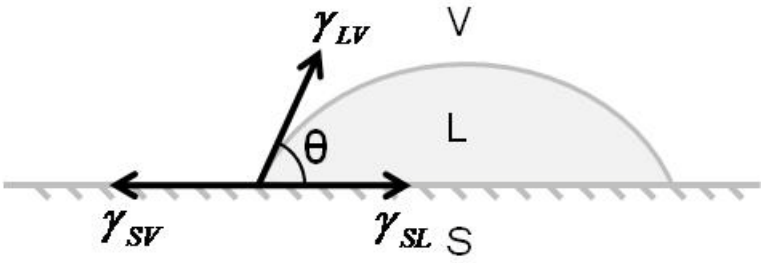

Figure 3.2. A droplet on a solid surface

By generalizing Eq. (3-9), small changes in Helmholtz free energy for multiple interfaces can be determined. If the temperature and the individual phase volumes are constant for the case in Fig. 3.2,

$$
\begin{aligned}
dF &= \sum_i u_i (dn_i^{LV} + dn_i^{SV} + dn_i^{SL}) + \sum_i u_i (dn_i^{S} + dn_i^{L} + dn_i^{V}) \\
&\quad + \gamma_{SV} dA_{SV} + \gamma_{LV} dA_{LV} + \gamma_{SL} dA_{SL}
\end{aligned}
\tag{3-10}
$$

If there is no mass transfer with surrounding, the number of moles remains unchanged,

$$
(dn_i^{LV} + dn_i^{SV} + dn_i^{SL}) + (dn_i^{S} + dn_i^{L} + dn_i^{V}) = dn_{iT} = 0, \tag{3-11}
$$

Then one has

$$
dF = +\gamma_{SV} dA_{SV} + \gamma_{LV} dA_{LV} + \gamma_{SL} dA_{SL} \tag{3-12}
$$

By the geometry

$$dA_{SV} = -dA_{SL} = \frac{1}{\cos\theta} dA_{LV} \tag{3-13}$$

Substituting Eq. (3-12) into Eq. (3-13) and rearranging gives

$$\frac{\partial F}{\partial A_{SL}} = \gamma_{SL} - \gamma_{SV} + \gamma_{LV} \cos\theta \tag{3-14}$$

At equilibrium, F has to be a minimum with respect to dA_{SL} and consequently $\partial F / \partial A_{SL} = 0$ and Eq. (3-14) can be rewritten

$$\gamma_{LV} \cos\theta = -\gamma_{SL} + \gamma_{SV} \tag{3-15}$$

This is called Young's equation. For this equation to be valid, it is assumed that there is no adsorption at the interfaces. Another assumption is to neglect the additional effect of line tension that may be caused by a linear excess of free energy due to the appearance of the junction of three different matters. In fact, it was found that the effect of line tension is negligible in contact angle measurements for drops with a radius larger than a few millimeters [83].

3.2.1.3 Finding the interfacial tension

Eq. (3-15) can be used to find interfacial tension between solid and liquid, γ_{SL} with known values of γ_{SV} and γ_{LV}, but cannot be used directly to determine either γ_{SV} or γ_{LV} when the other value is known unless one has the information of γ_{SL}. The main sources of the interfacial tensions are the London dispersion forces due to the intermolecular potential and polar forces due to the polarity of molecules in terms of acidity and basicity and expressed the sum of them.

$$\gamma_{12} = \gamma_{12}^{d} + \gamma_{12}^{AB} \tag{3-16}$$

where 1 and 2 indicates two materials in contact. There are several theories to express γ_{12} in terms of γ_1^d, γ_2^d, γ_1^{AB}, and γ_2^{AB} such as Fowkes theory [84,85], Wu theory [86], and Van Oss Theory [87,88]. In Fowkes theory

$$\gamma_{12} = \gamma_{11} + \gamma_{22} - 2(\sqrt{\gamma_{11}^{d}\gamma_{22}^{d}} + \sqrt{\gamma_{11}^{AB}\gamma_{22}^{AB}}) \tag{3-17}$$

Wu theory uses harmonic means rather than geometric means, so that

$$\gamma_{12} = \gamma_{11} + \gamma_{22} - 2(\frac{2\gamma_{11}^{d}\gamma_{22}^{d}}{\gamma_{11}^{d} + \gamma_{22}^{d}} + \frac{2\gamma_{11}^{AB}\gamma_{22}^{AB}}{\gamma_{11}^{AB} + \gamma_{22}^{AB}}) \tag{3-18}$$

Van Oss Theory further divides the polar component into two parts: the surface energy due to acidic interaction, γ^{A} and due to basic interaction, γ^{B}.

$$\gamma_{12} = \gamma_{12}^{d} + \gamma_{12}^{A} + \gamma_{12}^{B} \tag{3-19}$$

In the interfacial region, the acid components on surface theoretically have polar interactions with basic components on the other surface and vice versa. In the similar way to Fowkes theory

$$\gamma_{12} = \gamma_{11} + \gamma_{22} - 2(\sqrt{\gamma_{11}^{d}\gamma_{22}^{d}} + \sqrt{\gamma_{11}^{A}\gamma_{22}^{B}} + \sqrt{\gamma_{11}^{B}\gamma_{22}^{A}}) \tag{3-20}$$

Combining Eqs. (3-17), (3-18), and (3-19) with Eq. (3-15) and rearranging them give following relationships, respectively

$$\frac{\gamma_{LV}(\cos\theta + 1)}{2} = \sqrt{\gamma_{LV}^{d}\gamma_{SV}^{d}} + \sqrt{\gamma_{LV}^{AB}\gamma_{SV}^{AB}} \tag{3-21}$$

$$\frac{\gamma_{LV}(\cos\theta + 1)}{4} = \frac{\gamma_{LV}^{d}\gamma_{SV}^{d}}{\gamma_{LV}^{d} + \gamma_{SV}^{d}} + \frac{\gamma_{LV}^{AB}\gamma_{SV}^{AB}}{\gamma_{LV}^{AB} + \gamma_{SV}^{AB}} \tag{3-22}$$

$$\frac{\gamma_{LV}(\cos\theta + 1)}{2} = \sqrt{\gamma_{LV}^{d}\gamma_{SV}^{d}} + \sqrt{\gamma_{LV}^{A}\gamma_{SV}^{B}} + \sqrt{\gamma_{LV}^{B}\gamma_{SV}^{A}} \tag{3-23}$$

Through these equations one can determine the surface tension of a solid surface and its component using 2 known liquid probes for Eqs. (3-21) and (3-22), and 3 for Eq. (3-23). If the solid does not have polarity, one liquid probe is sufficient for this purpose.

3.2.1.4 Contact angle hysteresis

There are three types of contact angles: (i) static contact angle, which is the contact angle when the droplet is stationary (at equilibrium stage); (ii) advancing contact angle, which is the contact angle when the contact line is advancing to a new position over a dry solid surface; (iii) receding contact

angle, which is the contact angle when the contact line is receding into the region previously wet by the liquid. (ii) and (iii) are together called dynamic contact angle. These values are not often the same and the difference between advancing and receding contact angles is called contact angle hysteresis. There are several factors that cause this hysteresis such as impurities, roughness, and heterogeneity of a surface, adsorption and permeability of a liquid to the surface, and rotation of polar groups of surface depending on polarity of liquid. Especially the effect of roughness on hysteresis has been studied extensively being inspired by the hierarchical structure of natural lotus leaves and their self cleaning effect [13].

Thermodynamically contact angle hysteresis can be considered as a measure of energy dissipation during the flow of a droplet along a solid surface [2, 3]. Low hysteresis means that small energy dissipation is required for a droplet to move or flow. Many studies used the tilting method to determine the advancing and receding contact angle with another hysteresis indicator, roll-off tilting angle where the droplet starts to roll. However, in the tilting method, since advancing and receding contact angles are determined through one droplet where advancing interfacial tension may affect receding contact angle as well as advancing contact angle and vice versa, it may not be a good method to find advancing or receding interfacial tension.

Another way to study contact angle hysteresis is the sessile drop method in which liquid is supplied or withdrawn so that one can observe advancing and receding contact angles, respectively while a contact line moves [90-92]. However, it is tricky to use these contact angles to calculate the interfacial tensions because a droplet may not be at the equilibrium state and the angle may be affected by the droplet speed. Nevertheless, contact angle measurement system based on the sessile drop method was developed and employed to study the contact line speed dependence of contact angles and to find the interfacial tension of the material in section 3.3-3.5 .

3.2.2 The Theory on the Contacts Between Solids

The following theoretical treatment is based on the references [15,89,93].

3.2.2.1 Hertz model

The mathematical theory for the general three-dimensional contact problem was first given by Hertz for isotropic linear elastic material [78]. Including linear elasticity, several assumptions are made that

the surfaces in contact are perfectly smooth, that there is no frictional force and that surfaces of bodies in contact can be expressed in equations of the second degree.

Imagine that two bodies are in mathematical contact (i.e. unstressed and undeformed) so that the common normal line lies parallel to the applied force as shown in Fig. 3.3.; the common tangent plane is the xy plane and the common normal line is the z axis

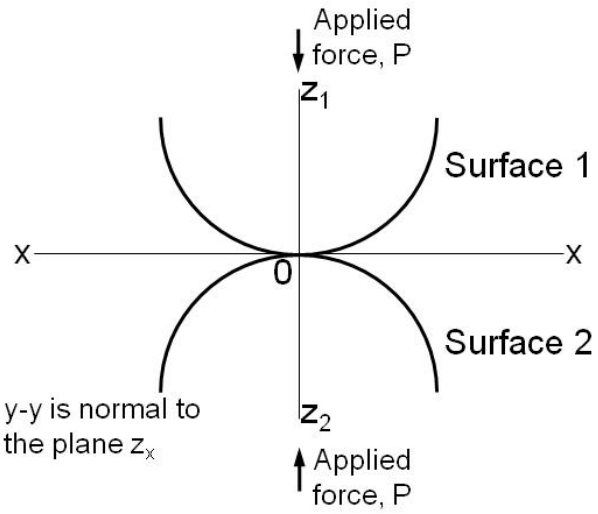

Figure 3.3. Mathematical contact of two bodies whose surfaces can be expressed in equations of the second degree

Let's consider the upper surface first. The general equation of the second degree is

$$ax^2 + by^2 + cz^2 + 2fyz + 2gzx + 2hxy + 2ux + 2vy + 2wz + d = 0 \tag{3-24}$$

At the origin, $x = y = z = 0$ and then $d = 0$. Differentiating Eq. (3-24) with respect to x and y, respectively, gives,

$$2ax + 2cz\frac{\partial z}{\partial x} + 2fy\frac{\partial z}{\partial x} + 2gz + 2gx\frac{\partial z}{\partial x} + 2hy + 2u + 2w\frac{\partial z}{\partial x} = 0 \tag{3-25}$$

$$2by + 2cz\frac{\partial z}{\partial y} + 2fz + 2fy\frac{\partial z}{\partial y} + 2gx\frac{\partial z}{\partial y} + 2hx + 2v + 2w\frac{\partial z}{\partial y} = 0 \tag{3-26}$$

At the origin, $x = y = z = \frac{\partial z}{\partial x} = \frac{\partial z}{\partial y} = 0$ and then $u = v = 0$. Therefore, Eq. (3-24) can be written as

$$ax^2 + by^2 + cz^2 + 2fyz + 2gzx + 2hxy + 2wz = 0 \tag{3-27}$$

Differentiating Eqs. (3-24) and (3-25) with respect to x and y, respectively, and Eq.(3-24) once more with respect to y,

$$2a + 2cz\frac{\partial^2 z}{\partial x^2} + 2c(\frac{\partial z}{\partial x})^2 + 2fy\frac{\partial^2 z}{\partial x^2} + 2g\frac{\partial z}{\partial x} + 2g\frac{\partial z}{\partial x} + 2gx\frac{\partial^2 z}{\partial x^2} + 2w\frac{\partial^2 z}{\partial x^2} = 0 \tag{3-28}$$

$$2b + 2cz\frac{\partial^2 z}{\partial y^2} + 2c(\frac{\partial z}{\partial y})^2 + 2f\frac{\partial z}{\partial y} + 2f\frac{\partial z}{\partial y} + 2fy\frac{\partial^2 z}{\partial y^2} + 2gx\frac{\partial^2 z}{\partial y^2} + 2w\frac{\partial^2 z}{\partial y^2} = 0 \tag{3-29}$$

$$2c\frac{\partial z}{\partial x}\frac{\partial z}{\partial y} + 2cz\frac{\partial^2 z}{\partial x \partial y} + 2f\frac{\partial z}{\partial x} + 2fy\frac{\partial^2 z}{\partial x \partial y} + 2g\frac{\partial z}{\partial y} + 2gx\frac{\partial^2 z}{\partial x \partial y} + 2h + 2w\frac{\partial^2 z}{\partial x \partial y} = 0 \tag{3-30}$$

At the origin, $x = y = z = \frac{\partial z}{\partial x} = \frac{\partial z}{\partial y} = 0$, and substituting this into Eqs. (3-28), (3-29), and (3-30) gives, respectively

$$2a + 2w\frac{\partial^2 z}{\partial x^2} = 0 \rightarrow \frac{\partial^2 z}{\partial x^2} = -\frac{a}{w} \tag{3-31}$$

$$2b + 2w\frac{\partial^2 z}{\partial y^2} = 0 \rightarrow \frac{\partial^2 z}{\partial y^2} = -\frac{b}{w} \tag{3-32}$$

$$2h + 2w\frac{\partial^2 z}{\partial x \partial y} = 0 \rightarrow \frac{\partial^2 z}{\partial x \partial y} = -\frac{h}{w} \tag{3-33}$$

Let $z = f(x, y)$ then, by using the Taylor's series, we can obtain the approximation to Eq. (3-27) around the origin point ($x = y = 0$). then

$$z = f(\partial x, \partial y) = f(0,0) + \partial x f_x(0,0) + \partial y f_y(0,0)$$
$$+ \frac{1}{2!}\{\partial x^2 f_{xx}(0,0) + 2\partial x \partial y f_{xy}(0,0) + \partial y^2 f_{yy}(0,0)\} \quad (3\text{-}34)$$
$$+ \textit{higher order terms (neglected)}$$

where $f_x = \frac{\partial z}{\partial x}$, $f_y = \frac{\partial z}{\partial y}$, $f_{xx} = \frac{\partial^2 z}{\partial x^2}$, $f_{yy} = \frac{\partial^2 z}{\partial y^2}$, and $f_{xy} = \frac{\partial^2 z}{\partial x \partial y}$. Since it is the approximation around the origin, we can replace ∂x and ∂y by x and y, respectively. Substituting $f(0,0) = f_x(0,0) = f_y(0,0) = 0$ and Eqs (3-31), (3-32), and (3-33) into Eq (3-34) gives

$$z = f(x,y) = \frac{1}{2}\{-\frac{a}{w}x^2 - \frac{2h}{w}xy - \frac{b}{w}y^2\} \quad (3\text{-}35)$$

In any given plane parallel to the xy plane in Fig. 3.3, z is constant, and then Eq (3-35) is an ellipse with its principal axes rotated with respect to its coordinate axes. If we rotate axes so that the principal axes are aligned with the coordinate axes, the xy term will vanish.

$$x = X\cos\theta + Y\sin\theta \quad (3\text{-}36)$$

$$y = -X\sin\theta + Y\cos\theta \quad (3\text{-}37)$$

Substituting Eqs (3-36) and (3-37) into Eq (3-35) gives

$$\begin{aligned} z = -\frac{1}{2}\{ & X^2(\frac{a}{w}\cos^2\theta + \frac{b}{w}\sin^2\theta - \frac{2h}{w}\cos\theta\sin\theta) \\ & + Y^2(\frac{a}{w}\sin^2\theta + \frac{b}{w}\cos^2\theta + \frac{2h}{w}\cos\theta\sin\theta) \\ & + XY(\frac{2a}{w}\sin\theta\cos\theta - \frac{2b}{w}\sin\theta\cos\theta + \frac{2h}{w}(\cos^2\theta - \sin^2\theta)\} \\ = \alpha \times X^2 + \beta \times Y^2 & - XY\{(\frac{a-b}{w})\sin 2\theta + \frac{h}{w}(\cos 2\theta)\} \end{aligned} \quad (3\text{-}38)$$

where α and β are constants. When $\tan 2\theta = \frac{b-a}{h}$, the XY term vanishes. By replacing X and Y by x and y, respectively, the equation becomes

$$z = Ax^2 + By^2 \quad (3\text{-}39)$$

where A and B are constants. We can determine these constants in terms of dimensions of the respective bodies. Let R and R' be the principle radii of curvature of the body for the planes $y = 0$ and $x = 0$, respectively. In the planes $y = 0$ and $x = 0$, we have $Ax^2 = z$ and $By^2 = z$, respectively. Here z is small enough so that $z^2 << z$. Therefore, we can assume that the curvature in the plane $y = 0$ is circular with a following equation,

$$x^2 + (z - R)^2 = R^2 \tag{3-40}$$

Reversely ignoring the second-order term of the small quantity z,

$$x^2 = 2Rz \tag{3-41}$$

Since $Ax^2 = z$, therefore,

$$A = \frac{1}{2R} \tag{3-42}$$

Similarly

$$B = \frac{1}{2R'} \tag{3-43}$$

Therefore, now we can have the equation for upper body by substituting Eqs. (3-42) and (3-43) into the equation (3-39):

$$z_1 = A_1 x^2 + B_1 y^2 = \frac{x^2}{2R_1} + \frac{y^2}{2R_1'} \tag{3-44}$$

And similarly we can find the equation for lower body

$$z_2 = A_2 x^2 + B_2 y^2 = \frac{x^2}{2R_2} + \frac{y^2}{2R_2'} \tag{3-45}$$

$|z_2|$ should be used instead of z_2 because it is minus, but for convenience z_2 is indicating $|z_2|$ in the rest of derivation. These equations can be combined into a single equation by adding.

$$z = z_1 + z_2 = (\frac{1}{2R_1} + \frac{1}{2R_2})x^2 + (\frac{1}{2R_1'} + \frac{1}{2R_2'})y^2 = Ax^2 + By^2 \tag{3-46}$$

Now we press two bodies together by applying force parallel to the z-axis as illustrated in Fig. 3.4. If the displacements at a point are w_1 and w_2, then for points inside the area of contact,

$$\begin{aligned}(z_1 + w_1) + (z_2 + w_2) &= \alpha \\ Ax^2 + By^2 + w_1 + w_2 &= \alpha\end{aligned} \tag{3-47}$$

While, outside the area of contact

$$(z_1 + w_1) + (z_2 + w_2) > \alpha \tag{3-48}$$

Note α is the sum of w_1 and w_2 at the origin.

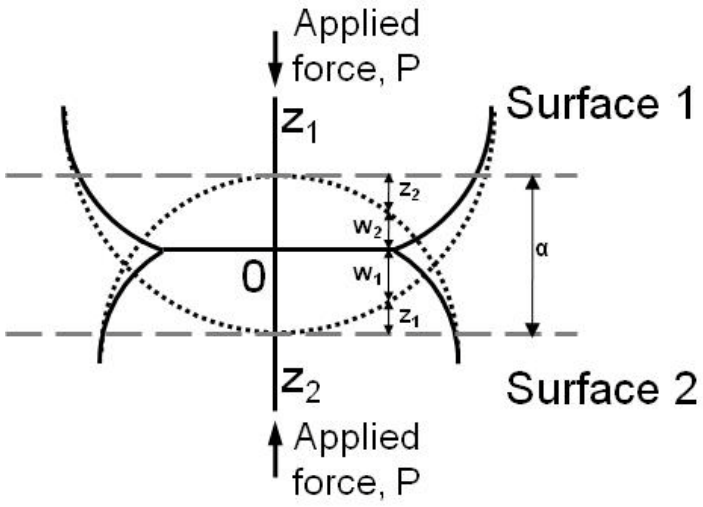

Figure 3.4. Two bodies in contact under the force applying parallel to the z-axis

Let the component of the pressure at a point (x', y') on the surface be $p(x', y')$. By assuming the surface to be plane, it can be shown that the deformation at a point (x, y) caused by this pressure is given by [94].

$$w(x, y) = \frac{1 - \nu^2}{\pi E} \times \frac{p(x', y')}{\sqrt{(x - x')^2 + (y - y')^2}} dx' dy' \tag{3-49}$$

where E and ν are elastic modulus and Poisson's ratio, respectively. By superposition theorem, the displacement at a point (x, y) caused by the distribution of pressure over an area A is given by

$$w(x,y)=\frac{1-\nu^2}{\pi E}\times\iint_A\frac{p(x',y')}{\sqrt{(x-x')^2+(y-y')^2}}dx'dy' \tag{3-50}$$

Substituting Eq. (3-50) into Eq. (3-47) gives

$$(\frac{1-\nu_1{}^2}{\pi E_1}+\frac{1-\nu_2{}^2}{\pi E_2})\times\iint_A\frac{p(x',y')}{\sqrt{(x-x')^2+(y-y')^2}}dx'dy'=\alpha-Ax^2-By^2 \tag{3-51}$$

where the subscripts 1 and 2 designate the elastic constants for the two bodies. A solution of Eq. (3-50) yields expression for the area of contact, the pressure distribution over the area, and the compression. This solution can be found by analogy with a problem in potential theory [95].

If an ellipsoid $x^2/a^2+y^2/b^2+z^2/c^2=1$ has a uniform volume, charge of density ρ, then it can be shown that the potential for points inside the ellipsoid is given by

$$\phi(x,y,z)=\pi\rho abc\int_0^\infty(1-\frac{x^2}{a^2+\psi}-\frac{y^2}{b^2+\psi}-\frac{z^2}{c^2+\psi})\frac{d\psi}{((a^2+\psi)(b^2+\psi)(c^2+\psi))^{1/2}} \tag{3-52}$$

If the ellipsoid is very much flattened, so that c becomes very small, we may write

$$\phi(x,y)=\pi\rho abc\int_0^\infty(1-\frac{x^2}{a^2+\psi}-\frac{y^2}{b^2+\psi})\times\frac{d\psi}{((a^2+\psi)(b^2+\psi)\psi)^{1/2}} \tag{3-53}$$

The potential can also be expressed in a more elementary way as

$$\phi(x,y,z)=\iiint_V\frac{\rho dx'dy'dz'}{\{(x-x')^2+(y-y')^2+(z-z')^2\}^{1/2}} \tag{3-54}$$

If the ellipsoid is very much flattened, z and z' cab be written as zero in Eq. (3-54). Therefore, the resulting expression is integrated with respect to z' over the range $\pm c\sqrt{1-(x'^2/a^2)-(y'^2/b^2)}$

$$\phi(x,y)=2\rho c\iint[1-\frac{x'^2}{a^2}-\frac{y'^2}{b^2}]^{1/2}\frac{dx'dy'}{\sqrt{(x-x')^2+(y-y')^2}} \tag{3-55}$$

Equating Eqs. (3-53) and (3-55) gives

$$\iint[1-\frac{x'^2}{a^2}-\frac{y'^2}{b^2}]^{1/2}\frac{dx'dy'}{\sqrt{(x-x')^2+(y-y')^2}}$$
$$=\frac{1}{2}\pi ab\int_0^\infty(1-\frac{x^2}{a^2+\psi}-\frac{y^2}{b^2+\psi})\times\frac{d\psi}{((a^2+\psi)(b^2+\psi)\psi)^{1/2}} \tag{3-56}$$

Comparing Eqs (3-51) with (3-56), it will be seen that, if the right-hand sides are viewed as quadratics in x and y, they have the identical form, while the left-hand sides are integrals of the same form

$$p(x,y)=k(1-\frac{x^2}{a^2}-\frac{y^2}{b^2})^{1/2} \tag{3-57}$$

Equating the integral $\iint_A p(x,y)dxdy$ to the total force *P*, compressing the two bodies gives $k=3P/2\pi ab$ so

$$p(x,y)=\frac{3P}{2\pi ab}(1-\frac{x^2}{a^2}-\frac{y^2}{b^2})^{1/2} \tag{3-58}$$

Substituting Eq. (3-58) into Eq. (3-51) and using Eq. (3-56)

$$\frac{P}{K\pi}\int_0^\infty(1-\frac{x^2}{a^2+\psi}-\frac{y^2}{b^2+\psi})\times\frac{d\psi}{((a^2+\psi)(b^2+\psi)\psi)^{1/2}}=\alpha-Ax^2-By^2 \tag{3-59}$$

where $\frac{1}{K}=\frac{3}{4}(\frac{1-\nu_1^2}{E_1}+\frac{1-\nu_2^2}{E_2})$ and K is called "effective modulus of the contacting particles"

As this expression must hold for all values of x and y within contact ellipse, expressions for α, A, and B can be obtained by equating coefficients on both sides of Eq. (3-59).

$$\delta=\frac{P}{K\pi}\int_0^\infty\frac{d\psi}{((a^2+\psi)(b^2+\psi)\psi)^{1/2}} \tag{3-60}$$

$$A=\frac{P}{K\pi}\int_0^\infty\frac{d\psi}{(a^2+\psi)((a^2+\psi)(b^2+\psi)\psi)^{1/2}} \tag{3-61}$$

$$B = \frac{P}{K\pi}\int_0^\infty \frac{d\psi}{(b^2+\psi)((a^2+\psi)(b^2+\psi)\psi)^{1/2}} \tag{3-62}$$

Note that A and B are geometric factors, $(1/2R_1 + 1/2R_2)$ and $(1/2R_1'+1/2R_2')$ given by Eq. (3-46). The constants a and b appeared in Eq. (3-60) are generally unknown, and are determined from the known geometric factors A and B through Eqs. (3-61) and (3-62).

3.2.2.2 Two spheres in contact by Hertz model

In case of two spheres whose radiuses are R_1 and R_2 in contact

$$\frac{1}{A} = \frac{1}{B} = (\frac{1}{2R_1} + \frac{1}{2R_2})^{-1} = 2(\frac{R_1R_2}{R_1+R_2})^{-1} = 2R \tag{3-63}$$

where R is called combined radii. Eqs. (3-61) and (3-62) become identical and can be written

$$A = B = \frac{1}{2R} = \frac{P}{K\pi}\int_0^\infty \frac{d\psi}{(a^2+\psi)^2\psi^{1/2}} \tag{3-64}$$

Also Eq. (3-60) can be written

$$\delta = \frac{P}{K\pi}\int_0^\infty \frac{d\psi}{(a^2+\psi)\psi^{1/2}} \tag{3-65}$$

where a is the radius of contact area. Note in case of two spherical surfaces, contact area has the shape of a circle. By putting $\psi^{1/2} = \rho$

$$\frac{1}{2R} = \frac{P}{K}\int_0^\infty \frac{2d\rho}{(a^2+\rho^2)^2} = \frac{P}{K\pi}\frac{\pi}{2a^3} \qquad \rightarrow a^3 = \frac{PR}{K} \tag{3-66}$$

$$\delta = \frac{P}{K\pi}\int_0^\infty \frac{2d\rho}{a^2+\rho^2} = \frac{P}{K\pi}\frac{\pi}{a} \qquad \rightarrow \delta = \frac{P}{Ka} \tag{3-67}$$

3.2.2.3 Two spheres in contact by JKR model

According to the Hertz model, it is the distribution of elastic forces that determines the equilibrium geometry of two solids in contact ignoring other factors such as friction. However, under light loading,

surface energy which is required energy to generate new surface can make a significant contribution, especially when the materials in contact are soft. Johnson et al [5] modified the Hertz theory on two spheres in contact taking the surface energy of the solid into account and developed the so-called JKR theory. The theory was basically derived from a balance of the three energy terms: (i) U_E, elastic energy associated with the deformation of the sphere, (ii) U_M, potential energy associated with the displacement of P load, and (iii) U_S, interfacial energy associated with adhesive bond at interface.

The total energy of the system can be written as

$$E_{Total} = U_S + U_E + U_M \tag{3-68}$$

At equilibrium, E_{Total} has to be a minimum with respect to A and consequently $\partial E_{Total} / \partial A = 0$.

$$\frac{\partial}{\partial A} E_{Total} = -w + \frac{\partial}{\partial A}(U_E + U_M) = 0 \tag{3-69}$$

where w is the work of adhesion, which is the energy spent in separating the two materials at the interface. Since the elastic energy is a state function that is path-independent, we can use a hypothetical deformation history that takes place in two stages as shown in Fig. 3.5.

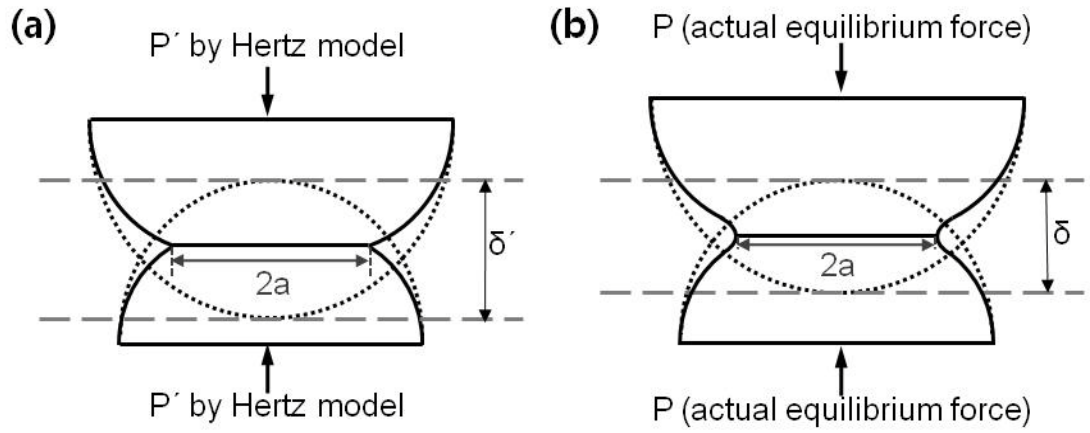

Figure 3.5. Two stages in hypothetical deformation history: (a) Neglecting the surface energy, two spheres are loaded against each other following the Hertz model, (b) Turning on surface interaction and keeping the contact radius constant, the two spheres are unloaded until the equilibrium state.

In the first stage neglecting the surface energy-induced force, the system is loaded until the contact area becomes $A = \pi a^2$ as illustrated in Fig. 3.5(a). The elastic energy associated with this portion of the deformation from mathematical contact, U_1 is

$$U_1 = \int_0^{\delta'(a)} P' d\delta \tag{3-70}$$

where P' and δ' define the load and displacement neglecting adhesive interactions (following the Hertz model) in the first hypothetical stage.

In the second stage of the hypothetical deformation process, the contact radius is fixed due to interfacial interactions, and the displacement (or load) decreases until it is equal to the value of interest (= value at equilibrium state) as illustrated in Fig. 3.5(b). Looking at the deformed profile of each sphere immediately outside the contact area, it is shown that in the second stage two spheres meet at the interface perpendicularly with the contact surface due to the adhesive force while in the previous stage they meet tangentially to each other. The energy, U_2, associated with this portion of deformation is

$$U_2 = \int_{P'}^{P} P d\delta \Big|_a \tag{3-71}$$

This quantity can be rewritten if we use the definition of compliance: $C = (\partial\delta/\partial P)\big|_a$, Assuming C is constant at a given contact area.

$$U_2 = \int_{P'}^{P} P d\delta \Big|_a = C \int_{P'}^{P} P dP \Big|_a = C\left(\frac{P^2}{2} - \frac{P'^2}{2}\right) \tag{3-72}$$

Then the overall elastic energy is determined as the sum of U_1 and U_2

$$U_E = U_1 + U_2 = \int_0^{\delta'} P' d\delta + C\left(\frac{P^2}{2} - \frac{P'^2}{2}\right) \tag{3-73}$$

The mechanical potential energy is determined by the distance over which the load has been moved, or $U_M = -P\delta$. Since we assumed that compliance is constant.

$$C = \frac{\delta' - \delta}{P' - P} \tag{3-74}$$

Therefore, we have

$$U_M = -P\{(\delta'-C(P'-P)\} \tag{3-75}$$

Substituting Eqs. (3-73) and (3-75) into Eq. (3-69) gives

$$\begin{aligned} w &= \frac{\partial}{\partial A}(U_E + U_M) = \frac{\partial}{\partial A}[\int_0^{\delta'} P' d\delta + C(\frac{P^2}{2} - \frac{P'^2}{2}) - P\{(\delta'-C(P'-P)\}] \\ &= \frac{\partial}{\partial A}\int_0^{\delta'} P' d\delta - \frac{(P-P')^2}{2}\frac{\partial C}{\partial A} - C(P'-P)\frac{\partial P'}{\partial A} - P\frac{\partial \delta'}{\partial A} + \{C(P'-P) - \delta'\}\frac{\partial P}{\partial A} \end{aligned} \tag{3-76}$$

Note that A was determined by P' in the first hypothetical deformation not by P. So we can consider $\partial P / \partial A = 0$. Therefore, we have

$$w = \frac{\partial}{\partial A}\left(\int_0^{\delta'} P' d\delta\right) - \frac{(P-P')^2}{2}\frac{\partial C}{\partial A} - C(P'-P)\frac{\partial P'}{\partial A} - P\frac{\partial \delta'}{\partial A} \tag{3-77}$$

By using the following two expressions:

$$w = \frac{\partial}{\partial A}\left(\int_0^{\delta'} P' d\delta\right) = P'\frac{\partial \delta'}{\partial A} \tag{3-78}$$

$$\frac{\partial \delta'}{\partial A} = \frac{\partial \delta'}{\partial P'}\frac{\partial P'}{\partial A} = C\frac{\partial P'}{\partial A} \tag{3-79}$$

Resulting equation is

$$w = -\frac{(P-P')^2}{2}\frac{\partial C}{\partial A} = -\frac{(P-P')^2}{4\pi a}\frac{\partial C}{\partial a} \tag{3-80}$$

According to the Hertz model $P' = Ka^3 / R$. C can be approximated by generalizing contact between a flat, rigid, and cylindrical indenter and an half-spaced elastic layer into one between two curved elastic half-spaces as shown in Fig. 3.6.

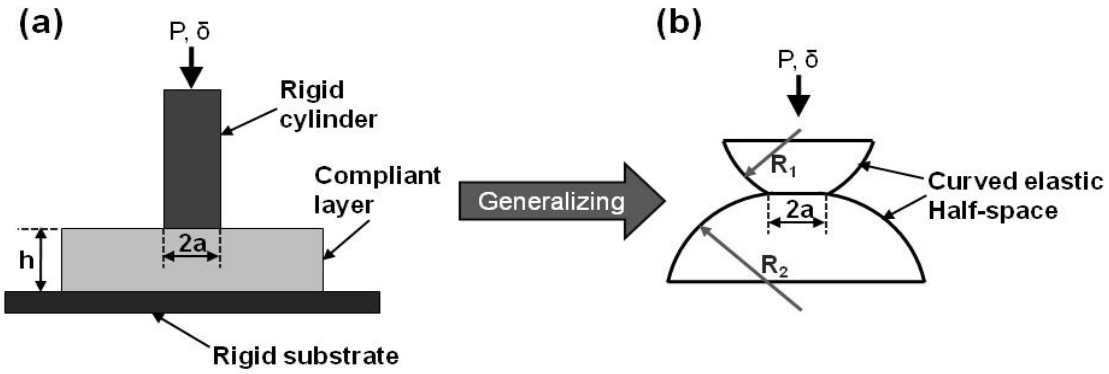

Figure 3.6. Contact (a) between a flat, rigid, and cylindrical indenter and an half-spaced elastic layer and (b) between two curved elastic half-spaces

In case of Fig. 3.6(a), the contact radius, a remains equal to the punch radius as the indenter is pushed into the half-space ($a/h \approx 0$). For light indenting, compliance, C is constant as follow:

$$C = \frac{\delta}{P} = \frac{1}{2E^* a} \tag{3-81}$$

where E^* is effective modulus of the elastic half-space (i.e. $E^* = (1-\nu^2)/E$). In case of Fig. 3.6(b), the displacement fields in the two half-spaces are added to one another. With the hypothesis that the contact area between the two materials remains fixed, the overall compliance is still given by Eq. (3-81) [96], with an effective modulus that involves the elastic constants of both half-spaces: (i.e. $1/E^* = (1-\nu_1^{\,2})/E_1 + (1-\nu_2^{\,2})/E_2 = 4/3K$)

Substituting $P' = Ka^3/R$ and Eq. (3-81) into Eq. (3-80) gives

$$w = -\frac{(P - Ka^3/R)^2}{4\pi a}\frac{\partial}{\partial a}\left(\frac{1}{2E^* a}\right) = \frac{(P - Ka^3/R)^2}{6\pi a^3 K} \tag{3-82}$$

If we solve Eq. (3-82) with respect to a^3 we have

$$a^3 = \frac{R}{K}\{P + 3\pi wR \pm \sqrt{(3\pi wR)^2 + 6\pi RPw}\} \tag{3-83}$$

Physically $a^3 > 0$, therefore, it is necessary to take only plus sign from ± in the equation. The result is

$$a^3 = \frac{R}{K}\{P + 3\pi wR + \sqrt{(3\pi wR)^2 + 6\pi RPw}\} \tag{3-84}$$

This is the well-known JKR equation. When $w = 0$, this reverts to the simple Hertz equation $a^3 = PR/K$.

3.2.2.4 Relation between work of adhesion and surface energy

Work of adhesion between materials a and b, w_{ab} is directly related to their surface energies. Opening the interface between a and b generates two new surfaces of A and B. Therefore, from the energy point of view, we can write

$$w_{ab} = \gamma_{aa} + \gamma_{bb} - \gamma_{ab} \tag{3-85}$$

Using the Eqs. (3-17) and (3-18), we have

$$w_{ab} = 2(\sqrt{\gamma_{aa}^d \gamma_{bb}^d} + \sqrt{\gamma_{aa}^{AB} \gamma_{bb}^{AB}}) \tag{3-86}$$

$$w_{ab} = 2(\frac{2\gamma_{aa}^d \gamma_{bb}^d}{\gamma_{aa}^d + \gamma_{bb}^d} + \frac{2\gamma_{aa}^{AB} \gamma_{bb}^{AB}}{\gamma_{aa}^{AB} + \gamma_{bb}^{AB}}) \tag{3-87}$$

If the materials are the same, both Eqs. (3-86) and (3-87) give

$$w_{aa} = 2(\gamma_{aa}^d + \gamma_{aa}^{AB}) = 2\gamma_{aa} \tag{3-88}$$

In following sections (3.3-3.5), JKR-type indentation tests were performed on PDMS with different speeds: Hemispherical PDMS was brought (loading) into contact with PDMS sheet and detached (unloading) and the experimental data were fitted to the JKR equation. Hysteresis behaviour that occurs between load and unloading portions was discussed with its dependence on the contacting/separating speed.

3.3 Experimental Setup

To study the surface property of materials such as surface energy and adhesion hysteresis, contact angle measurement system and micro-indentation system with real-time bottom view set-up (so-

called JKR-type apparatus) were developed using LabVIEW and Matlab. Main hardware components of the systems are listed with their detail specification in table 3-1.

Table 3-1. Main components of the experimental setup

Components	Specification
1 axis motorized micro linear stage (MFA-CC, Newport)	- Travel range : 25mm - Minimum increment : 100nm - Resolution: 17.5nm - Maximum Speed(mm/s): 2.5 - Backlash: 2μm
CCD camera (scA1000-30FM, Basler)	- Monochrome - Connection type: 1394b - CCD size: 1/3in - Resolution: 1034 X 779 pixels - Frame rate: 30fps - Lens mount type: C-Mount
Inverted microscope (OMM300T, Omano)	- Includes objectives(4X, 10X, 20X, 40X, and 80X) - Epi-Kohler lighting with aperture iris diaphragm and field iris diaphragm.
Micro load cell (GSO-25, Transducer Techniques)	- Capacity range: 25g - Hysteresis: 0.05% of capacity - Nonrepeatability: 0.05% of capacity - Zero Balance: 1.0% of capacity - Deflection: 0.1016 mm /25g
Motorized syringe pump (NE-1000, New Era Pump Systems)	- Speed range: 0.73 μL/hr (1cc syringe) to 2100 ml/hr (60cc syringe)

3.3.1 Contact Angle Measurement

The developed contact angle measurement system is based on the sessile drop technique. It mainly consists of a motorized syringe pump, 500ul syringe, thin polymer tube, syringe barrel, barrel holder, 1 axis motorized micro linear stage, xy axis manual stage, sharp needle (outer diameter of 0.21mm), LED light and CCD camera installed with microscope objective lens. The schematic of the set-up is shown in Fig. 3.7.

The motorized syringe pump enables one to control the supply of water with a specified speed as well as the volume of droplet. For advancing contact angle measurement, water is supplied so that droplet volume increases forwarding the contact line to new dry surface. Similarly for receding contact angle measurement water is withdrawn in a opposite manner so that droplet volume decreases pulling the contact line back to the region previously wet by the liquid. An objective lens magnifies

the view of droplet and an LED light enhances contrast significantly to increase the accuracy in analyzing process. A sequence of pictures of the droplet can be recorded by the LabVIEW program typically at a certain frame rate depending on the liquid flow speed to avoid huge set of images. These pictures are analyzed by the custom-developed MATLAB code to determine contact angle, droplet volume, and diameter of SL (solid-liquid) interface.

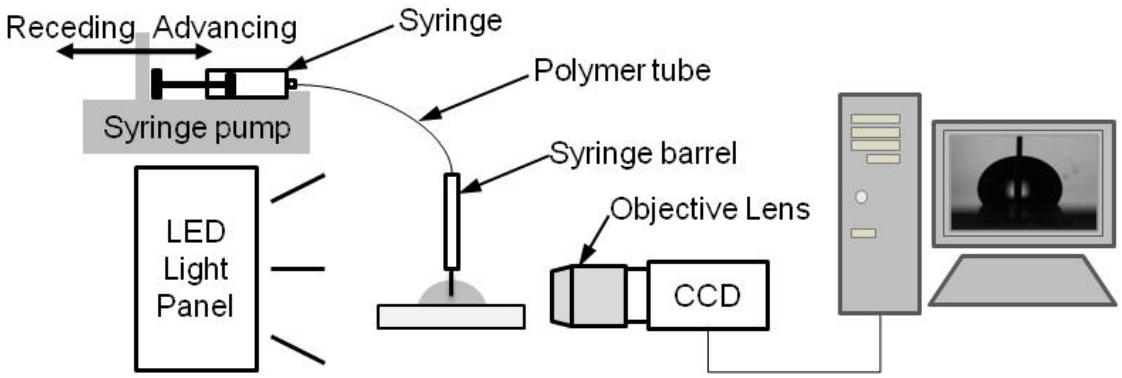

Figure 3.7. Schematic of contact angle measurement system

The custom-developed MATLAB code is based on the edge detection algorithm [97]. An edge in an image is a boundary or contour where a remarkable change takes place in some physical aspect of an image such as the surface reflection, color, illumination, or the distances of the visible surfaces from the camera. In most cases, these changes appear to be variation of intensity in grey-level image. The fundamental concept for edge detection is the utilization of the partial derivatives or Laplacian of the image function $f(x, y)$ and some filters corresponding to methods with a proper threshold value. By adopting this technique, the shape and volume of the droplet can be recognized, and then contact angle, and diameter of SL interface can be determined. Among the various edge detection algorithms, such as Sobel method, Roberts method, and Laplacian-based methods, Canny method [97] was employed for this study. Since the Canny method uses two threshold values to detect strong and weak edges, and includes the weak edges in the output only if they are connected to strong edge, weak edges are likely to be detected while noise are less likely to be included in output. Detailed mathematical expression can be found in [97].

Fig. 3.8. shows the key procedure of determining the diameter of SL interface, droplet volume, and left and right contact angles. Except defining the area of interest, all procedures are done

automatically.

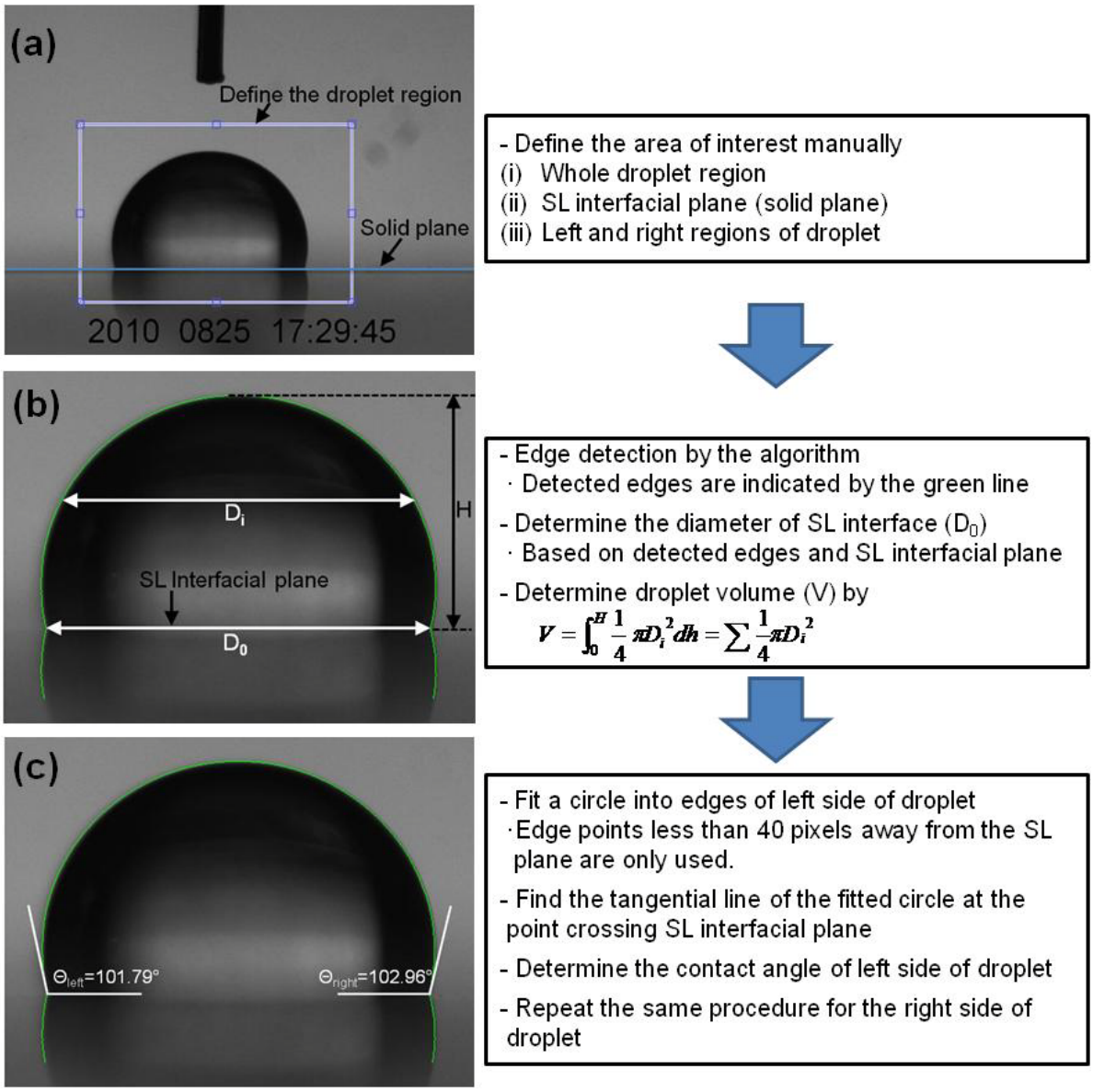

Figure 3.8. Procedure of determining the diameter of SL interface, droplet volume, and left and right contact angles; (a) Original image, (b) Edge detected image, and (c) Edge detected image with contact angles.

3.3.2 JKR-type Indentation

JKR-type indentation apparatus is developed consisting mainly of a micro load cell, manual stage, motorized micro linear stage, inverted microscope, anti-vibration table and CCD cameras, as

illustrated in Fig. 3.9(a). An half sphere indenting tip is brought into the contact with flat counter surface (loading) and is detached (unloading) in sequence. The manual stage is used to position the indenting tip in xy plane to align with objective lens and camera prior to performing indentation. A motorized stage is installed to control z-axis movement of tip with resolution of 100nm during indentation. The whole set up is developed on the anti-vibration table.

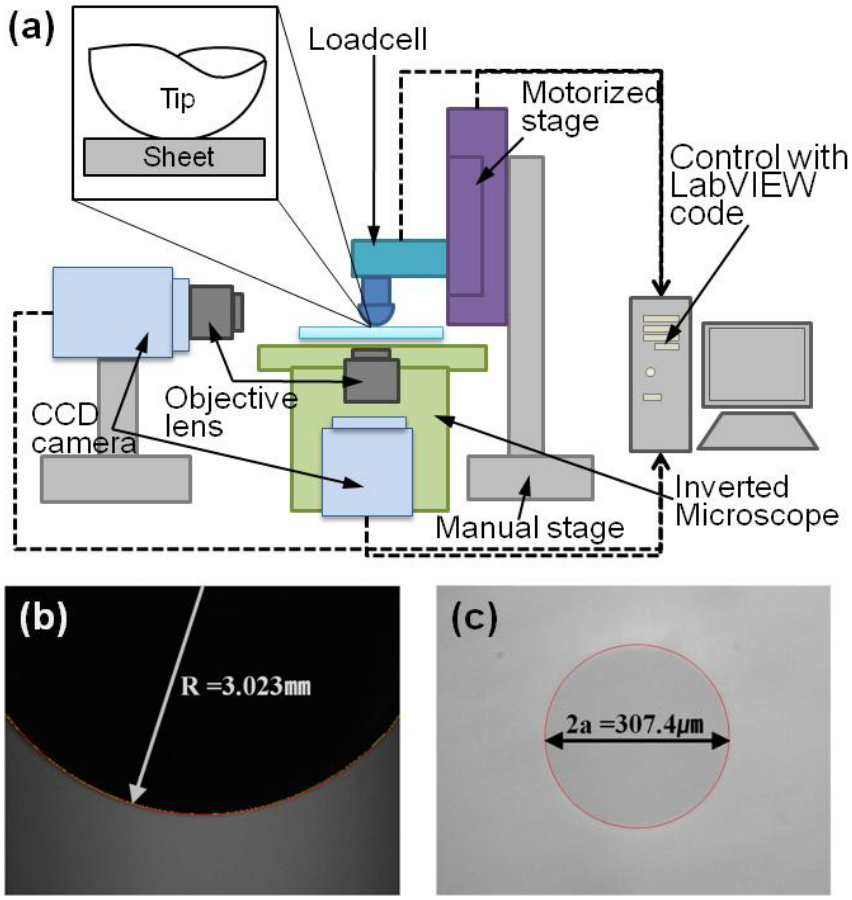

Figure 3.9. (a) Schematic of JKR-type indentation apparatus, (b) Radius of the tip measurement, and (c) the radius of the contact area

The CCD camera installed in the inverted microscope results in a spatial resolution of 1.035μm/pixel. Another camera is installed to capture the side view of the tip. Custom-developed LabVIEW code controls the movement of linear stage and records the loading, time, and displacement information as well as the side view of the tip and the bottom-view image of the contact spot simultaneously during the test. The radius of the tip (Fig. 3.8(b)) and the radius of the contact area (Fig. 3.8(c)) are extracted

from the images by computational edge detection techniques used in the contact angle measurement system.

3.4 Test

3.4.1 Sample Preparation

The PDMS (Sylgard Elastomer 184, Dow Corning Corporation) solution was prepared by mixing the base and the cross-linker at the ratio of 10:1. Trapped air bubble resulted from stirring was removed in a desiccator by applying vacuum for 30min. The flat sheets were made by casting 2mL of the solution onto a microscope slide and curing at 90 °C for 1.5 hours in ambient air. The hemispherical tip was made through 2 steps. PDMS solution was poured into a hemispherical (radius of 3mm) shaped Teflon mold and then curing at 90 °C for 15 min. Since the resulting tip surface is rough another layer of solution was applied on top of it and cured at 90 °C for 1.5 hours in ambient air. The final tip radius was calculated within 1% error by the custom built Matlab code as illustrated Fig. 3.9(b)

3.4.2 Contact Angle

A sharp flat-end stainless steel needle (inner and outer diameters are 0.11 and 0.21mm respectively) was placed close to a PDMS flat sheet and 5μl of water was dispensed. Since the position of the needle is hard to keep being in the center of the droplet at the starting point, the needle had to be relocated to be in the center of the droplet so that the flow of the droplet was uniform all direction. Another 5μl of water was supplied to remove any effect caused by needle repositioning process. It was confirmed that water flows uniformly in all direction once needle is placed in the center of droplet. Images were recorded at a specified frame rate while 20μl of water was being dispensed and then the whole droplet was being aspirated subsequently at a predetermined droplet volume speed. The droplet speeds used are 300, 100, 10, and 2 μl/min. The tests were repeated three times for each case.

3.4.3 JKR-type Indentation

Indentation tests were performed with three types of stage movements: (i) step-wisely with a speed of 0.1 μm/s (The stage stops at every 0.05g increment and decrement point, waits for 30s, and moves for

the next increment or decrement point); (ii) continuously with a speed of 0.1 μm/s; (iii) continuously with a speed of 1 μm/s. PDMS hemisphere tip was translated by the linear stage at the specified motion to be brought into contact with PDMS flat sheet attached and supported by a microscope slide glass and withdrawn at the same speed. The total indentation depth was determined at a loading force of 0.5g. For quantitative analysis, three characteristic parameters were determined using the contact radius vs. force curves: (i) Effective modulus of the contacting surfaces, K; (ii) the work of adhesion, w; (iii) the maximum force required to separate the tip from the substrate, so-called pull-off force P_s. w and K were extracted by fitting the contact radius a and external force P of loading portion to Eq. (3-84) through the least square method. The tests were repeated three times for each case.

3.5 Results and Discussion

3.5.1 Contact Angle

The typical test results for each case are shown in Fig. 3.10. As shown, 5 points were selected where noticeable changes occur ; t_0: contact line starts to move forward, t_1: contact line stops moving, t_2: the volume of droplet starts to decrease, t_3: contact line starts to withdraw, and t_4: contact angle starts to decrease significantly or to be unstable. Based on these 5 points, the results were divided into 6 domains for 300μl/min, 200μl/min, and 10μl/min cases, and 5 regions for 2μl/min case where t_1 and t_2 overlaps.

Contact angle and volume increase while the contact line is stationary in the first region, showing that static and advancing contact angles are different at this point. The second region is characterized by a nearly constant contact angle, where advancing contact angle was determined as the average value in this region. The average speeds of contact lines in this region are calculated and inserted in Fig. 3.10. At the third region, the volume is maximum and the contact angle decreases and is stabilized from advancing to static. The fourth region is transition zone where contact angle changes from static to receding. Fifth regions are characterized by a nearly constant contact angle, where the receding contact angle is determined as the average value in this region. The sixth region is meaningless because drop size is so small that the needle affects the angles.

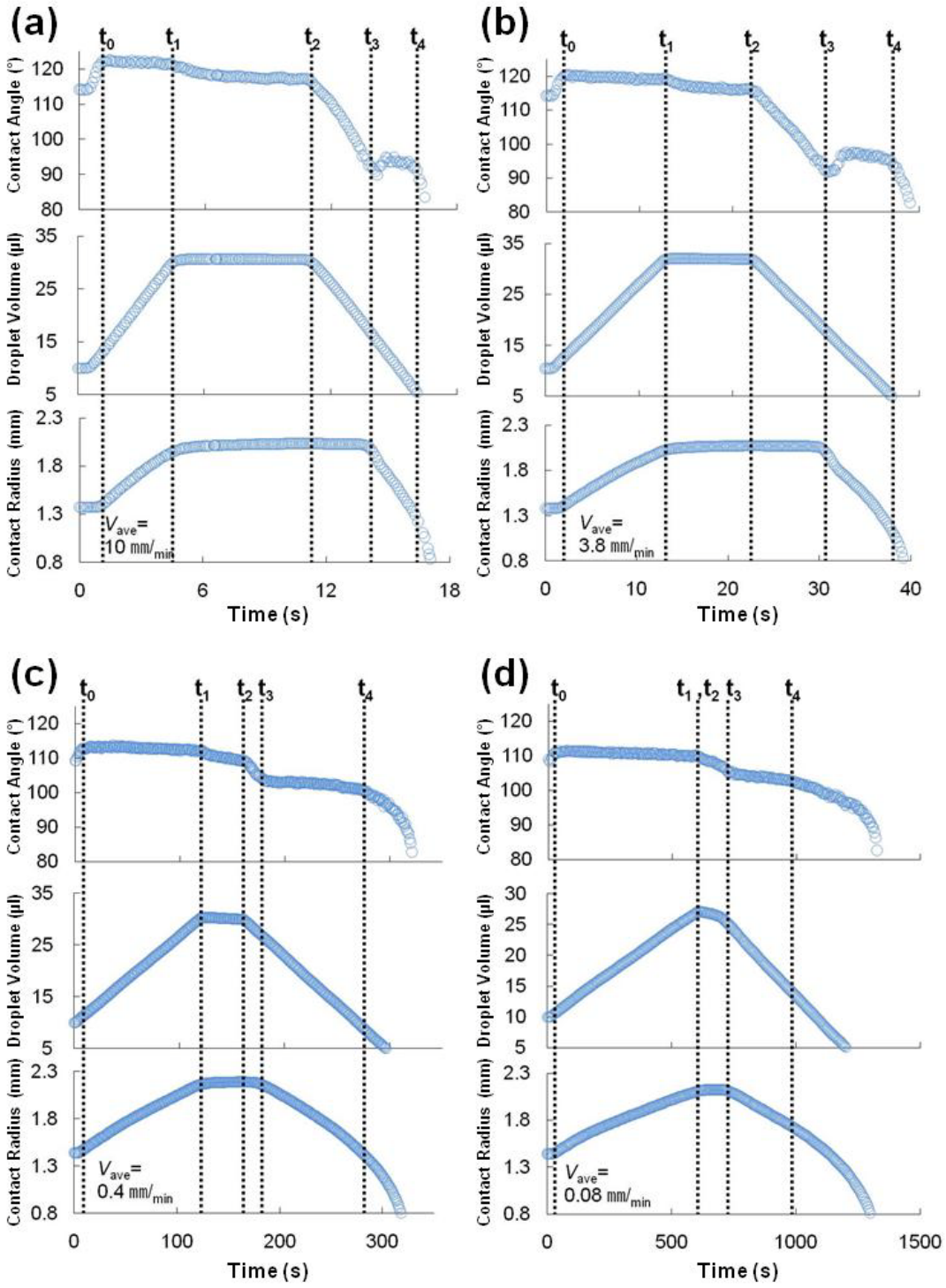

Figure 3.10. Contact angles, drop volume, and contact radius for (a) v=300µl/min, (b) v=100µl/min, (c) v=10µl/min, and (d) 2µl/min.

It is interesting that at high speeds (300 and 100 μl/min) the contact line pinned and jumped to a new location with sharp increment of contact angle when transferring from fourth to fifth regions while smooth transition occurs at low speeds (10 and 2 μl/min). Stick-slip pattern of receding liquid on a solid surface is described by Lam et al [92]. They explained that 'pinning' of the three-phase line could be due to a particularly strong interaction, e.g. a chemical bond. However, their case was repeated stick-slip which differs from non-repeating stick-slip observed here. The reason why speed-dependant stick-slip occurs is a hard question to answer and ambiguous, but that might be related with viscosity or friction of the water rather than chemical bonding.

The measured contact angles are summarized in the table 3.2 and depicted in Fig. 3. The dynamic contact angles of PDMS used in this study have been studied extensively by other researchers [98-100]. Advancing contact angle, θ_A ranges from 110° to 118° and receding contact angle, θ_R ranges from 82° to 106°. Only one value of static contact angle, θ_S was available as 105° from the literature review [100]. Our dynamic contact angle data are very similar to the literature values, but static data show slight difference. In fact, there is no clear boundary between static contact angle and advancing/receding contact angles. Some people use advancing and receding contact angles as upper and low bound of static one while some other people consider advancing contact angle as equilibrium static contact angle [90-92]. This may be one of the reasons why only 105° could be found from the literature review and its value is different from our data.

Table 3-2. Contact angles and surface energy depending on the flow rate

Flow rate (μl/min)	Average contact line speed (mm/min)	Contact angle (°)				Surface energy (mJ/m^2)			
		θ_S	θ_A	θ_R	θ_{Hys}	γ_S	γ_A	γ_R	γ_{Hys}
300	10	117.02±0.27	121.49±0.39	94.13±0.71	27.37	15.92	12.96	46.89	33.93
100	3.8	116.33±0.04	120.06±0.28	97.11±0.10	22.95	16.43	13.85	40.28	26.43
10	0.4	109.98±0.03	112.95±0.12	103.29±0.42	10.72	21.93	19.16	29.88	10.71
2	0.08	109.58±0.41	110.55±0.18	104.10±0.70	6.46	22.34	21.37	28.77	7.40

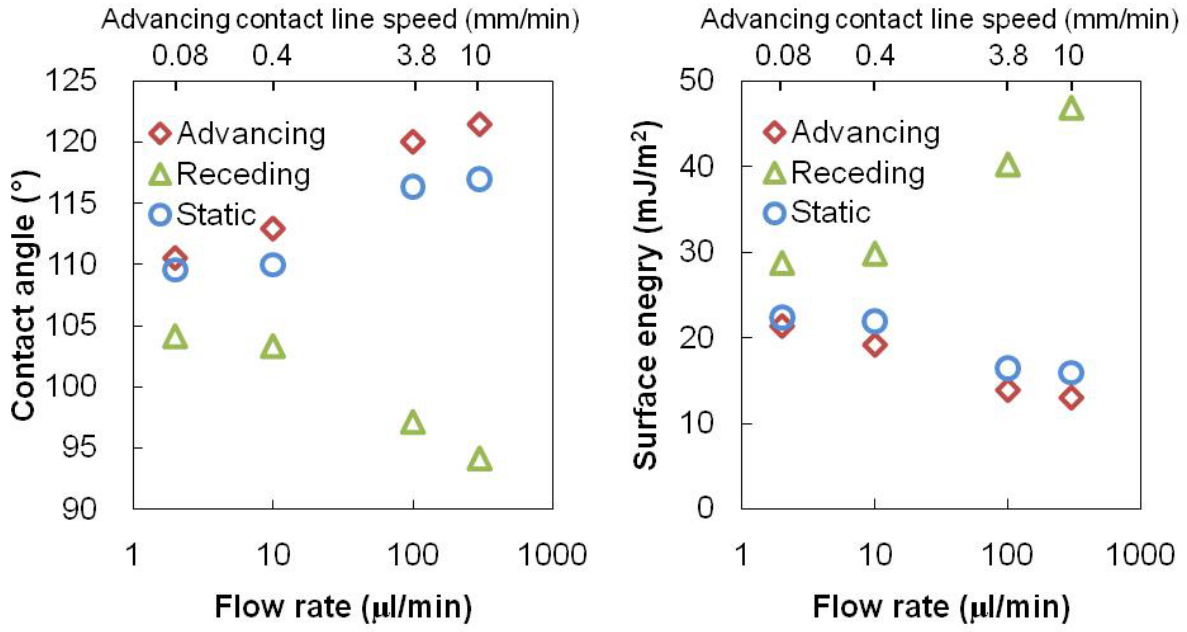

Figure 3.11. Contact angles and surface energy depending on the flow rate

As shown in the table 3.2, static contact angle as well as dynamic contact angles and their hysteresis depend on the rate of growth and diminishment of droplet. Tavana et al [90] reported that for liquids with a dynamic viscosity of well below 10 cP, neither advancing nor receding contact angle is influenced significantly by the rate of contact line movement up to 12 mm/min, while for more viscous liquids, high rate causes the advancing contact angle to increase and the receding contact angle to decrease. However, we have different results from them: the dynamic contact angles of water whose viscosity is under 10 cP are affected by contact line speed ranging from 0.08 to 10 mm/min. Tavana et al used different liquids and surfaces [90]. Riddiford and co-workers studied contact angles of water on silicone, glass plate and PTFE surfaces and observed two contact line speed regions where advancing contact angle is constant; below the speed of 1 mm/min and above the speed of 7 mm/min [101]. Between the two plateaus, the advancing contact angle increases linearly with increasing the rate of contact line movement. Our case is closer to that of Riddiford's study as shown in Fig. 3.11. Therefore, we may conclude that the interaction between a solid surface and a liquid plays a role in determining the effect of contact line speed by providing upper and lower boundaries of dynamic contact angles. Riddiford [101] explained this phenomenon by considering time spent for water molecules to orient on a solid surface: at very low speed, water molecules at the

contact line have sufficient time to settle on the surface while at very high speed they are in the state of completion of disorientation.

At the beginning of the previous paragraph, it was mentioned that even the static contact angle depends on the speed of contact line; values from high droplet speeds are even higher than advancing contact angles from low speeds. This is against the concept that advancing contact angle is an upper bound of static contact angle. It was presumed that static contact angles from high speeds are under thermodynamically metastable condition while static contact angles from low speeds are stable and close to the actual value. At the stationary state, disoriented water molecules caused by the high speeds of contact line movement may not be able to develop full orientation because they are confined by neighboring molecules, resulting in metastable state.

The effective surface energies are calculated based on Wu method for each case and shown in the table 3-2. It should be noted that PDMS does not have polar component and consequently water droplet is enough to find surface energy of PDMS. PDMS is known to have the surface energy of 20~24mJ/m^2 [102-104], which is consistent with our data from static contact angle tests and slightly higher than the values from advancing contact angles at two low speeds (2 and 10 μl/min). We can conclude that low droplet speed should be used for measuring static contact angle.

With the assumption of the quasi equilibrium at the speed of 2μl/min, advancing and receding contact angles can be considered as "static" advancing and receding contact angles and used to apply the Young equation. Riddiford and co-workers also considered the contact angles in the lower plateau region where the angles barely changed as the thermodynamic equilibrium angles to be used in the Young equation [101]. At this low speed range, the hysteresis is relatively small.

For the high speed range, it is not proper to calculate surface energy with Young equation. However, instead of surface energy, we may evaluate the hysteresis of the effective work of adhesion or energy release rate between PDMS and water by using the equation if the contact line moves at constant speed; [89].

$$g_s = w_s = \gamma_{LV} + \gamma_{SV} - \gamma_{LV} = \gamma_{LV}(1+\cos\theta_s) \quad \text{At equilibrium} \quad (3\text{-}89)$$

$$g_A = w_A = \gamma_{LV} + \gamma_{SV} - \gamma_{LV} - \gamma_{A\_diss} = \gamma_{LV}(1+\cos\theta_A) \quad \text{At advancing} \quad (3\text{-}90)$$

$$g_R = w_R = \gamma_{LV} + \gamma_{SV} - \gamma_{LV} + \gamma_{R\_diss} = \gamma_{LV}(1+\cos\theta_R) \quad \text{At receding} \quad (3\text{-}91)$$

γ_{A_diss} and γ_{R_diss} are the energy-dissipated term to accommodate both chemical and physical effects such as liquid speed and play a role in the force balance that determines the contact angle [89]. One can find the dissipated energy per unit area during the process of advancing and receding by subtracting Eq. (3-90) from Eq. (3-91). The assumption is that the dissipation of energy occurs at the vicinity of the contact line. The obtained value is the sum of all kinds of energy dissipations. However, energy dissipations caused by the viscosity of liquid (i.e. speed effect) and by chemical potential (i.e the change of interfacial or surface tension) might be evaluated in the following way. First, find the energy dissipation ($\gamma_{diss\_low\_speed}$) for very low speed which we consider only from the change of surface tension. Second, find the energy dissipation ($\gamma_{diss\_high\_speed}$) for high speed considered to be from both physical and chemical effects. Subtracting $\gamma_{diss\_high\_speed}$ by $\gamma_{diss\_low\_speed}$, one can extract energy dissipation by physical effect.

3.5.2 JKR-type Indentation

Typical contact radius versus loading force curves are depicted in Fig. 3.12 with JKR equation (Eq. 3-84) fittings to the loading portion of each case. For the stepwise indentation tests, data right after 30s waiting time were used assuming the system is in equilibrium at these points. Fitting parameters are tabulated in the table 3.3. Surface energy, γ and elastic modulus, E were also calculated using Eq. (3-88) and the definition of K, respectively. Poisson's ratio was assumed to be 0.5 in determining elastic modulus.

As shown in Fig. 3. 12., the fitted JKR curves appeared to be in a good agreement with loading data. However, regardless the stage movement, hysteresis take places and unloading curves deviate from loading. Attempts to fit JKR equation to unloading data with different fitting parameters were made, but none of them was successful. JKR theory assumes that the material is linear elastic and work of adhesion is constant. Therefore, ideal materials are supposed to show zero hysteresis [15]. PDMS is considered to be purely elastic in macroscopic level and shows linear stress-strain behaviour under small strain as discussed in Chapter 2. The observed hysteresis may be attributed to the possible increase of work of adhesion caused by existence of free chains on PDMS surface.

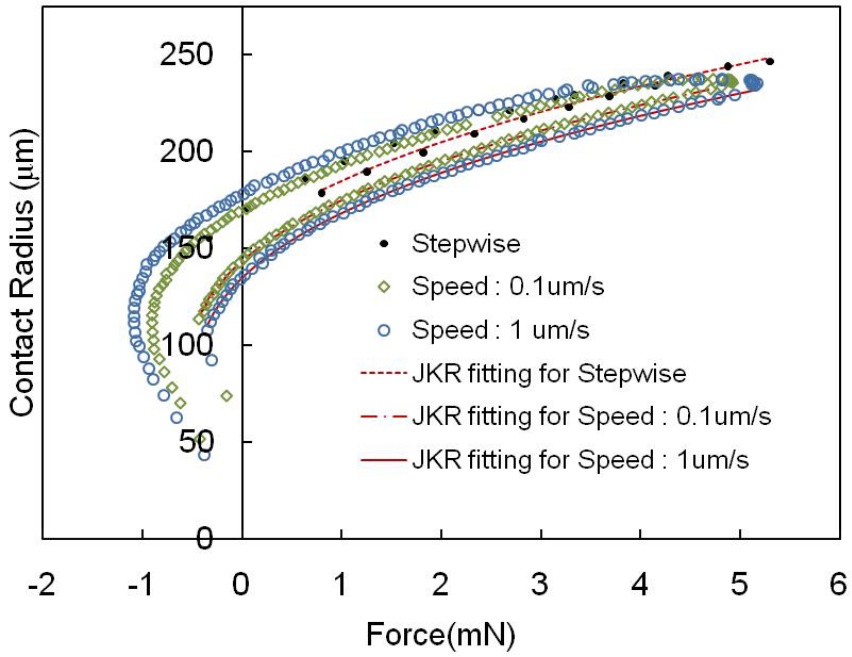

Figure 3.12. Load and contact radius curves and JKR fittings to the loading portions.

Table 3-3. Characteristic parameters from JKR-type indentation tests

Motion	$w(mJ/m^2)$	$\gamma(mJ/m^2)$	$K(MPa)$	$E(MPa)$	$P_s(\mu N)$
Stepwise	45.8±1.18	22.9±0.59	2.01±0.01	2.26±0.01	N/A
0.1 μm/s	39.8±0.97	19.9±0.49	2.03±0.01	2.28±0.01	880±35
1 μm/s	33.5±0.91	16.75±0.45	2.06±0.02	2.32±0.02	1070±14

While chains inside of bulk material are confined, those on the surface are relatively free and allowed to move. Viscous behaviours at the micro-scale have been observed on the PDMS surface [105-107]. Some researchers investigated the effects of polymer chains of PDMS surface on adhesion. Kroner et al attributed oligomers transfered from PDMS to sapphire ball to the reduced adhesion during the repeated indentation test [105]. Galliano et al studied the effect of chain length of PDMS on adhesion [107,108]. They also confirmed migration of free polymer chain from PDMS to glass surface with an atomic force microscope and accounted for contact hysteresis with energy dissipation determined by the degree of crosslinking. Since chains on the PDMS surface are less confined, they move and spread during the indenting (loading) and help to develop intimate molecular contact.

Eventually they start to migrate between contact surfaces and entangle with each other as loading increases. Because of these intimate contact and entanglement, more energy is required to separate the two surfaces causing loading-unloading hysteresis. Also if we assume that higher pressure between surfaces strengthen chain entanglement, degree of entanglement decreases along the contact radius direction and therefore, so does work of adhesion. This would be the reason why JKR equation cannot fitted into the unloading data.

As seen in the Fig. 3. 12, the hysteresis increases with the speed. It can also be explained by the chain entanglement. During the chain disentangling process, it would be the friction between chains that mainly causes the hysteresis. Under the condition of low speed or step-wise tests, free chains on the surfaces have enough time to flow and develop intimate molecular contact during the loading and disentangle relatively smoothly during the unloading. However, if the speed is too fast for the chains to either rearrange or pass through each other gradually, they rather hinder contact between surfaces during loading and may become a source of excess frictions in molecular level and even consume more energy due to their breakage during unloading. This might be the reason why loading curve is lower and unloading curve is higher at high speed. Using the same concept, the observation of higher pull-off force P_s at the speed of 1μm/s than that at 0.1μm/s can be explained. (Pull-off force is only available at dynamic test not at the step-wise test.)

Among the characteristic quantities obtained from the loading curves, resulted surface energy falls within the literature range [102-104] at the stepwise test and deceases as the test speed increases. For the elastic modulus, it was observed that modulus increases as the speed increases but by very small amount. This would be also attributed to the free chains on PDMS surface. Under loading, the free chains flow gradually and it takes time for the chains to settle and develop intimate contact between surfaces. Therefore, we can also consider that free chains form a very thin viscous layer. This likely viscous layer on the surface would affect in estimating the elastic modulus by JKR fitting depending on the testing speed. However, the effect would be minor considering its thickness as shown in the Table 3.3. This suggests that even though the material is considered elastic in bulk, there may be a possible thin viscous layer on the surface due to free chains.

3.6 Conclusion

As the importance of surface property of material increases, it is necessary to use proper tools to investigate them. The two most common experimental methods characterizing surface energy of material were developed and tested with PDMS as a model material. The tests verified the two experimental set-up with theories on contact angle and JKR equation showing a good agreement with literature values of PDMS surface energy under (quasi) equilibrium state (at very low speed test condition). From the dynamics tests, hysteresis behaviour and deviation of surface energy were qualitatively discussed with their dependence on the rate of contact development and sources. It is very complicated to incorporate the sources of hysteresis such as chemical interaction between contacting material, existence of free chains on the surface, chain entanglement, and viscosity of material into analytical equation. However, considering its applications such as self cleaning surface, adhesives, and interaction between materials in micro fabrication, these hysteresis behaviour and methods to manipulate should be investigated further.

Chapter 4
Summary and Recommendation

4.1 Summary

Two independent studies were performed. In the first study, custom 2D and 3D digital image correlation codes were developed to measure the deformation of materials accurately regardless of test conditions. Supplementary algorithms (sub-pixel and smoothing algorithms) were also developed to enhance the accuracy of measurement. Developed codes were employed in two applications:

(i) Determining the stress-strain behaviour of soft material under large deformation.

DIC technique was further optimized for large strain measurement regarding referencing scheme and image frame rate. Dynamic referencing scheme with a proper frame rate in DIC analysis is more suitable than fixed referencing scheme in large deformation. A series of comparative studies with conventional method and FEM results suggest that optimized DIC technique can yield accurate stress strain curve even in large deformation region while conventional methods showed poor performance as the deformation becomes significant. This is because DIC technique is robust to the slip between the sample and the grips while the accuracy of conventional test scheme is highly affected by the slip. Based on the stress strain curve obtained from DIC technique, an empirical constitutive equation of PDMS across large deformation domain was proposed considering its significant strain-hardening behaviour. The proposed constitutive equation was verified by the virtual tension test using FEM simulation. The optimized DIC technique and analysis method used here may be able to be applied to the studies of other elastomers, gels and biological tissues.

(ii) Possibility of diagnosis of malignant tissue in breast.

A breast phantom was made with agarose and gelatin gel. This phantom contains an inclusion with different stiffness. Elastic moduli of outer and inclusion parts were altered by changing gelatin concentration. 2D and 3D displacement and strain fields of phantom under deformation were generated by DIC and DVC, respectively. With the aid of smoothing algorithm, both DIC and DVC techniques were able to detect the existence of inclusion mimicking tumour and its position in the phantom accurately. The ratio of elastic modulus of inclusion to that of outer material and the diameter of inclusion in phantom were also estimated from strain field. This study shows the potential

application of DIC and DVC algorithms combined with smoothing function to diagnosing pathological tissue within the body in-vivo.

In the second study, two most common experimental set-ups (contact angle measurement system and JKR-type indentation tester) characterizing surface energy and adhesion of material were also custom-developed. Using PDMS as a model material, dynamic tests were performed with both apparatuses: In contact angle measurement, water flow of both advancing and receding modes was controlled by changing droplet volume rate (μl/min) while in JKR-type indentation test, the speed of contact between surfaces was controlled by changing the speed of linear stage. When contact between materials develops under very low speed test condition, surface energy obtained from both experiments are almost the same and within the range of literature value verifying the experimental set-ups. From the tests with high speed, hysteresis behaviour and deviation of surface energy were observed and qualitatively discussed with their dependence on the rate of contact development and sources such as chemical interaction between contacting material, existence of free chains on the surface, chain entanglement, and viscosity of material.

4.2 Recommendations

For the future work, the following recommendations are suggested:

(i) In DIC-based strain measurement, smoothing algorithm was adopted to increase the accuracy of its performance in generating the strain field. However, smoothing algorithm may distort the original data. Therefore, the effect of smoothing parameter that controls the degree of smoothing should be further investigated and optimized in the way that accuracy of tracking should be maximized while the distortion of the data be kept minimal. Even though GCV method introduced in the section 2.2.3 was used for this purpose, it would be worth trying to optimize it with respect to pixel-spacing between neighboring points tracked by DIC, because GCV method does not take absolute spacing between neighboring data into consideration.

(ii) The relationship between friction and adhesion has been one of the conventional issues in studying interaction between two materials in contact. Therefore, friction test set-up should be added to JKR-type indentation test set-up for in-depth and comprehensive analysis in contact problem. To do so, a linear stage for later movement and another load cell are required.

(iii) During the JKR-type indentation test, accessible visual information is limited to 2D images of contact spot between materials. Employing fluorescent microscope instead of normal optical

microscope, 3D images of contact region can be obtained. Furthermore applying DVC code developed in this work may allow 3 dimensional measurement of deformation during the contact. Since the fluorescent particles should be mixed with object material for this purpose. the adhesion behaviour of material may be altered by these particle. Nevertheless, it should be able to give deep insight of contact behaviour of materials.

Bibliography

[1] D.H. Lewis and D.J. Castleberry, “An assessment of recent advances in external maxillofacial materials,” *The Journal of Prosthetic Dentistry*, vol. 43, 1980, pp. 426-432.

[2] F. Li, Y. Su, D. Shi, and C. Wang, “Comparison of human articular cartilage and polyvinyl alcohol hydrogel as artificial cartilage in microstructure analysis and unconfined compression,” *Advanced Polymer Processing*, vol. 87-88, 2010, pp. 188-193.

[3] A. Nava, E. Mazza, M. Furrer, P. Villiger, and W.H. Reinhart, “In vivo mechanical characterization of human liver,” *Medical image analysis*, vol. 12, 2008, pp. 203-216.

[4] M. Kauer, V. Vuskovic, J. Dual, G. Szekely, and M. Bajka, “Inverse finite element characterization of soft tissues,” *Medical image analysis*, vol. 6, 2002, pp. 275-287.

[5] M.S. Thompson, H. Schell, J. Lienau, and G.N. Duda, “Digital image correlation: a technique for determining local mechanical conditions within early bone callus,” *Medical engineering & physics*, vol. 29, 2007, pp. 820-823.

[6] D. Zhang and D.D. Arola, “Applications of digital image correlation to biological tissues,” *Journal of biomedical optics*, vol. 9, 2004, pp. 691-699.

[7] T.C. Chu, W.F. Ranson, and M. a Sutton, “Applications of digital-image-correlation techniques to experimental mechanics,” *Experimental Mechanics*, vol. 25, 1985, pp. 232-244.

[8] B.D. Lucas and T. Kanade, “An iterative image registration technique with an application to stereo vision,” *Imaging*, vol. 130, 1981, pp. 121-129.

[9] M. Kass, A. Witkin, and D. Terzopoulos, “Snakes: Active contour models,” *International Journal of Computer Vision*, vol. 1, 1988, pp. 321-331.

[10] N.P. Papanikolopoulos, “Selection of features and evaluation of visual measurements during robotic visual servoing tasks,” *Journal of Intelligent & Robotic Systems*, vol. 13, 1995, pp. 279-304.

[11] J. Lewis, “Fast template matching,” *Vision Interface*, 1995, pp. 120–123.

[12] Y. Guo, G. Liu, Y. Xiong, and Y. Tian, “Study of the demolding process—implications for thermal stress, adhesion and friction control,” *Journal of Micromechanics and Microengineering*, vol. 17, 2007, pp. 9-19.

[13] B. Bhushan and Y.C. Jung, “Natural and biomimetic artificial surfaces for superhydrophobicity, self-cleaning, low adhesion, and drag reduction,” *Progress in Materials Science*, vol. 56, 2011, pp. 1-108.

[14] H. Gao, X. Wang, H. Yao, S. Gorb, and E. Arzt, “Mechanics of hierarchical adhesion structures of geckos,” *Mechanics of Materials*, vol. 37, 2005, pp. 275-285.

[15] K. Johnson, K. Kendall, and A. Roberts, “Surface energy and the contact of elastic solids,” *Proceedings of the Royal Society of London. A. Mathematical and Physical Sciences*, vol. 324, 1971, pp. 301-313.

[16] F. Hild and S. Roux, “Digital Image Correlation: from displacement measurement to identification of elastic properties - a Review,” *Strain*, vol. 42, 2006, pp. 69-80.

[17] S. Mguil-touchal, F. Morestin, and M. Brunet, “Various experimental applcations of digital image correlation method,” *Contact and Structural Mechanics Laboratory. Laboratoire de Mécanique des Solides, University de Lyon*

[18] R. Hamam, F. Hild, and S. Roux, “Stress Intensity Factor gauging by digital image correlation: application in cyclic fatigue,” *Strain*, vol. 43, 2007, pp. 181-192.

[19] M.S. Kirugulige, H.V. Tippur, and T.S. Denney, “Measurement of transient deformations using digital image correlation method and high-speed photography: application to dynamic fracture,” *Applied optics*, vol. 46, 2007, pp. 5083-5096.

[20] D. Garcia, “Robust smoothing of gridded data in one and higher dimensions with missing values,” *Computational Statistics & Data Analysis*, vol. 54, 2010, pp. 1167-1178.

[21] G. Wahba, “Spline Models for Observational Data,” *Society for Industrial and Applied Mathematics*, 1990.

[22] H.L. Weinert, “Efficient computation for Whittaker–Henderson smoothing,” *Computational Statistics & Data Analysis*, vol. 52, 2007, pp. 959-974.

[23] W. Yueh, “Eigenvalues of several tridiagonal matrices,” *Applied Mathematics E-Notes*, vol. 5, 2005, pp. 66-74.

[24] G. Strang, “The discrete cosine transform,” *SIAM Review*, vol. 41, 1999, p. 135.

[25] U.S. Schwarz, N.Q. Balaban, D. Riveline, A. Bershadsky, B. Geiger, and S.A. Safran, “Calculation of forces at focal adhesions from elastic substrate data: the effect of localized force and the need for regularization,” *Biophysical journal*, vol. 83, 2002, pp. 1380-1394.

[26] C. Vaquette, C. Frochot, R. Rahouadj, S. Muller, and X. Wang, “Mechanical and biological characterization of a porous poly- L -lactic acid-co-ϵ-caprolactone scaffold for tissue engineering,” *Soft Materials*, vol. 6, 2008, pp. 25-33.

[27] B. Hinz, G. Celetta, J.J. Tomasek, G. Gabbiani, and C. Chaponnier, “Alpha-smooth muscle actin expression upregulates fibroblast contractile activity,” *Molecular biology of the cell*, vol. 12, 2001, pp. 2730-2741.

[28] T.R. Hoare and D.S. Kohane, “Hydrogels in drug delivery: Progress and challenges,” *Polymer*, vol. 49, 2008, pp. 1993-2007.

[29] C. Creton, “Pressure-sensitive adhesives : An Introductory Course,” *MRS Bulletin*, 2003, pp. 434-439.

[30] C.E. Kandow, P.C. Georges, P.A. Janmey, and K.A. Beningo, “Polyacrylamide hydrogels for cell mechanics: Steps toward optimization and alternative uses,” *Methods in Cell Biology*, vol. 83, 2007, pp. 29-46.

[31] D.M. Nelson, Z. Ma, K.L. Fujimoto, R. Hashizume, and W.R. Wagner, “Intra-myocardial biomaterial injection therapy in the treatment of heart failure: Materials, outcomes and challenges,” *Acta biomaterialia*, vol. 7, 2011, pp. 1-15.

[32] “Testing of rubber: determination of tensile strength at break, tensile stress at yield, elongation at break, and stress values in a tensile test,” *German Industry Standard*, DIN 53504, 1994.

[33] “Physical testing of rubber: Method for determination of tensile stress-strain properties,” *British Standard*, BS 903-A2, 1995.

[34] “Standard Test Method for Vulcanized Rubber and Thermoplastic Elastomers—Tension,” *Annual Book of ASTM Standards*, D412-06a, 2008.

[35] T. Aziz, M. Waters, and R. Jagger, “Analysis of the properties of silicone rubber maxillofacial prosthetic materials.,” *Journal of dentistry*, vol. 31, 2003, pp. 67-74.

[36] H. Kwon, A.D. Rogalsky, C. Kovalchick, and G. Ravichandran, “Application of digital image correlation method to biogel,” *Polymer Engineering and Science*, vol. 50, 2010, p. 1585–1593.

[37] F. Schneider, T. Fellner, J. Wilde, and U. Wallrabe, “Mechanical properties of silicones for MEMS,” *Journal of Micromechanics and Microengineering*, vol. 18, 2008, p. 065008.

[38] C.B. Churchill, J. A. Shaw, and M. A. Iadicola, “Tips and tricks for characterizing shape memory alloy wire: Part 2-Fundamental isothermal responses,” *Experimental Techniques*, vol. 33, 2009, pp. 51-62.

[39] J. Dournaux, S. Bouvier, A. Aouafi, and P. Vacher, “Full-field measurement technique and its application to the analysis of materials behaviour under plane strain mode,” *Materials Science and Engineering: A*, vol. 500, 2009, pp. 47-62.

[40] T.A. Berfield, J.K. Patel, R.G. Shimmin, P.V. Braun, J. Lambros, and N.R. Sottos, “Micro- and nanoscale deformation measurement of surface and internal planes via digital image correlation,” *Experimental Mechanics*, 2007, pp. 51-62.

[41] L.C.S. Nunes, “Shear modulus estimation of the polymer polydimethylsiloxane (PDMS) using digital image correlation,” *Materials & Design*, vol. 31, 2010, pp. 583-588.

[42] H. Lu and P.D. Cary, “Deformation measurements by digital image correlation: Implementation of a second-order displacement gradient,” *Experimental Mechanics*, vol. 40, 2000, pp. 393-400.

[43] S.R. Heinz and J.S. Wiggins, “Uniaxial compression analysis of glassy polymer networks using digital image correlation,” *Polymer Testing*, vol. 29, 2010, pp. 925-932.

[44] R. Cintron and V. Saouma, “Strain measurements with the digital image correlation system vic-2D,” *Architectural Engineering. University of Colorado,* 2008.

[45] “Standard Test Method for Linear-Elastic Plane-Strain Fracture Toughness of Metallic Materials,” *Annual Book of ASTM Standards*, E399-09, 2009.

[46] G. Emanuel. E, "Fracture mechanics: an introduction, " *Springer*, 2005.

[47] K.G. Sharp, G.S. Blackman, N.J. Glassmaker, A. Jagota, and C.-Y. Hui, “Effect of stamp deformation on the quality of micro contact printing: theory and experiment.,” *Langmuir : the ACS journal of surfaces and colloids*, vol. 20, 2004, pp. 6430-6438.

[48] J.C. Lotters, W. Olthuis, P.H. Veltink, and P. Bergveld, “The mechanical properties of the rubber elastic polymer poly dimethylsiloxane for sensor applications,” *Journal of Micromechanics and Microengineering*, vol. 7, 1997, pp. 145-147

[49] K. Khanafer, A. Duprey, M. Schlicht, and R. Berguer, “Effects of strain rate , mixing ratio , and stress – strain definition on the mechanical behavior of the polydimethylsiloxane (PDMS) material as related to its biological applications,” *Biomed Microdevices*, 2009, pp. 503-508.

[50] C. Chiang, C. Klin, and M. Ju, “An implantable capacitive pressure sensor for biomedical applications,” *Sensors and Actuators A: Physical*, vol. 134, 2007, pp. 382-388.

[51] T. Gervais, J. El-Ali, A. Günther, and K.F. Jensen, “Flow-induced deformation of shallow microfluidic channels,” *Lab on a chip*, vol. 6, 2006, pp. 500-507.

[52] L.R.J. Treloar, “The Physics of Rubber Elasticity,” *Oxford: Clarendon Press*, 1975.

[53] M. Mooney, “A theory of large elastic deformation,” *Journal of Applied Physics*, vol. 24, 1940, pp. 582-592.

[54] P.J. Blatz, “Strain energy function for rubberlike materials based on a generalized measure of strain,” *Journal of Rheology*, vol. 18, 1974, pp. 145-161.

[55] G. Gsell and J.J. Jonas, “Determination of the plastic behaviour of solid polymers at constant true strain rate,” *Journal of materials science*, vol. 14, 1979, pp. 583-591.

[56] R.D. Groot, A. Bot, and W.G.M. Agterof, “Molecular theory of strain hardening of a polymer gel: Application to gelatin,” *The Journal of Chemical Physics*, vol. 104, 1996, pp. 9202-9219.

[57] A. N. Gent, “Crystallization and the relaxation of stress in stretched natural rubber vulcanizates,” *Transactions of the Faraday Society*, vol. 50, 1954, p. 521-533.

[58] S. Toki, “Strain-induced crystallization of natural rubber as detected real-time by wide-angle X-ray diffraction technique,” *Polymer*, vol. 41, 2000, pp. 5423-5429.

[59] Statistics Canada, *Causes of death, 2007*, 2010.

[60] A. Jemal, R. Siegel, J. Xu, and E. Ward, “Cancer statistics, 2010,” *CA: a cancer journal for clinicians*, 2010.

[61] R. A. Smith, V. Cokkinides, and H.J. Eyre, “American Cancer Society guidelines for the early detection of cancer,” *CA: a cancer journal for clinicians*, vol. 56, 2006, pp. 11-25.

[62] J. Ophir, I. Cespedes, B. Garra, H. Ponnekanti, Y. Huang, and N. Maklad, “Elastography: Ultrasonic imaging of tissue strain and elastic modulus in vivo,” *European Journal of Ultrasound*, vol. 3, 1996, pp. 49-70.

[63] M. Doyley, “A freehand elastographic imaging approach for clinical breast imaging: system development and performance evaluation,” *Ultrasound in Medicine & Biology*, vol. 27, 2001, pp. 1347-1357.

[64] C.H. Lee, D.D. Dershaw, D. Kopans, P. Evans, B. Monsees, D. Monticciolo, R.J. Brenner, L. Bassett, W. Berg, S. Feig, E. Hendrick, E. Mendelson, C. D'Orsi, E. Sickles, and L.W. Burhenne, "Breast cancer screening with imaging: recommendations from the Society of Breast Imaging and the ACR on the use of mammography, breast MRI, breast ultrasound, and other technologies for the detection of clinically occult breast cancer," *Journal of the American College of Radiology : JACR*, vol. 7, 2010, pp. 18-27.

[65] P. Skrabanek, "Mass mammography. The time for reappraisal," *International Journal of Technology Assessment in Health Care*, vol. 5, 1989, pp. 423-430.

[66] H. Zhi, B. Ou, B.M. Luo, X. Feng, and Y.L. Wen, "Comparison of ultrasound elastography, mammography, and sonography in the diagnosis of solid breast lesions," *Journal of Ultrasound In Medicine*, vol. 26, 2007, pp. 807-815.

[67] T.J. Hall, "AAPM/RSNA physics tutorial for residents: topics in US: beyond the basics: elasticity imaging with US," *Radiographics*, vol. 23, 2003, pp. 1657-1671.

[68] J. Ophir, F. Kallel, T. Vargese, E. Konofagou, S.K. Alam, T. Krouskop, B. Garra, and R. Righetti, "Elastography," *Optical and Acoustical Imaging of Biological Media*, vol. 2, 2001, pp. 1193-1212.

[69] J. Ophir, S.K. Alam, B. Garra, F. Kallel, E. Konofagou, T. Krouskop, and T. Varghese, "Elastography: ultrasonic estimation and imaging of the elastic properties of tissues," *Proceedings of the Institution of Mechanical Engineers. Part H,* vol. 213, 1999, pp. 203-233.

[70] F. Lanza di Scalea, S.S. Hong, and G.L. Cloud, "Whole-field strain measurement in a pin-loaded plate by electronic speckle pattern interferometry and the finite element method," *Experimental Mechanics*, vol. 38, 1998, pp. 55-60.

[71] A. Lyshchik, T. Higashi, J.J. Mai, C. Pellot-barakat, M.F. Insana, and A.B. Brill, "Thyroid gland tumor diagnosis at US elastography [1]," *Head and Neck Imaging. Radiology*, 2005, pp. 202-237

[72] T. Rago, F. Santini, M. Scutari, A. Pinchera, and P. Vitti, "Elastography: new developments in ultrasound for predicting malignancy in thyroid nodules," *The Journal of clinical endocrinology and metabolism*, vol. 92, 2007, pp. 2917-2922.

[73] T. Krouskop, T. Wheeler, F. Kallel, and B. Garra, "Elastic moduli of breast and prostate tissues under compression," *Ultrasonic imaging*, Vol. 20, 1998, pp. 260-274

[74] K.J. Parker, M.M. Doyley, and D.J. Rubens, "Imaging the elastic properties of tissue: the 20 year perspective," *Physics in Medicine and Biology*, vol. 56, 2011, pp. R1-R29.

[75] B. Zhao, H. Zeng, Y. Tian, and J. Israelachvili, “Adhesion and detachment mechanisms of sugar surfaces from the solid (glassy) to liquid (viscous) states,” *Proceedings of the National Academy of Sciences of the United States of America*, vol. 103, 2006, pp. 19624-19629.

[76] L.C. Xu and C. A. Siedlecki, “Effects of surface wettability and contact time on protein adhesion to biomaterial surfaces,” *Biomaterials*, vol. 28, 2007, pp. 3273-3283.

[77] W.G. Brodbeck, J. Patel, G. Voskerician, E. Christenson, M.S. Shive, Y. Nakayama, T. Matsuda, N.P. Ziats, and J.M. Anderson, “Biomaterial adherent macrophage apoptosis is increased by hydrophilic and anionic substrates in vivo,” *Proceedings of the National Academy of Sciences of the United States of America*, vol. 99, 2002, pp. 10287-10292.

[78] H. Hertz, “On the contact of elastic solids,” *JourTialfur die reine und angewandte Matlumatilc*, vol. 92, 1881, pp. 156-171.

[79] X.D. Wang, Z.X. Shen, J.L. Zhang, H.F. Jiao, X.B. Cheng, X.W. Ye, L.Y. Chen, and Z.S. Wang, “Contact between submicrometer silica spheres.,” *Langmuir : the ACS journal of surfaces and colloids*, vol. 26, 2010, pp. 5583-5586.

[80] E. Charrault, C. Gauthier, P. Marie, and R. Schirrer, “Experimental and theoretical analysis of a dynamic JKR contact,” *Langmuir : the ACS journal of surfaces and colloids*, vol. 25, 2009, pp. 5847-5854.

[81] Y. Morishita, H. Morita, D. Kaneko, and M. Doi, “Contact dynamics in the adhesion process between spherical polydimethylsiloxane rubber and glass substrate,” *Langmuir : the ACS journal of surfaces and colloids*, vol. 24, 2008, pp. 14059-14065.

[82] C.A. Miller and P. Neogi, “Interfacial phenomena: equilibrium and dynamic effects, second edition,” *CRC Press, Taylor & Francis Group*, 2008.

[83] A. Mu and A.W. Neumann, “Measurements of line Tension for solid-liquid-vapor systems using drop size dependence of contact angles and its Correlation with solid-liquid interfacial tension,” *Langmuir*, vol. 16, 2000, pp. 2024-2031.

[84] F.M. Fowkes, “Attractive forces at interfaces,” *Industrial & Engineering Chemistry*, vol. 56, 1964, p. 40–52.

[85] F.M. Fowkes, “Chemistry and physics of interfaces,” *American Chemical Society*, 1965, pp. 1-12.

[86] S. Wu, “Calculation of interfacial tension in polymer systems,” *Journal of Polymer Science Part C: Polymer Symposia*, 1971, pp. 19-30.

[87] C. Van Oss, M. Chaudhury, and R. Good, “Monopolar surfaces,” *Advances in colloid and interface science*, vol. 28, 1987, p. 35–64.

[88] C.J. Van Oss, R.J. Good, and M.K. Chaudhury, “Additive and nonadditive surface tension components and the interpretation of contact angles,” *Langmuir*, vol. 4, 1988, pp. 884-891.

[89] K. Shull, “Contact mechanics and the adhesion of soft solids,” *Materials Science and Engineering: R: Reports*, vol. 36, 2002, pp. 1-45.

[90] H. Tavana and a Neumann, “On the question of rate-dependence of contact angles,” *Colloids and Surfaces A: Physicochemical and Engineering Aspects*, vol. 282-283, 2006, pp. 256-262.

[91] D. Kwok, T. Gietzelt, K. Grundke, H.J. Jacobasch, and A. Neumann, “Contact angle measurements and contact angle interpretation. 1. Contact angle measurements by axisymmetric drop shape analysis and a goniometer sessile drop technique,” *Langmuir*, vol. 13, 1997, pp. 2880–2894.

[92] C.N.C. Lam, R. Wu, D. Li, M.L. Hair, and A.W. Neumann, “Study of the advancing and receding contact angles : liquid sorption as a cause of contact angle hysteresis,” 2002, pp. 169-191.

[93] M.J. Puttock and E.G. Thwaite, “Elastic compression of spheres and cylinders at point and line contact,” *Industrial Research*, 1969.

[94] J. Prescott, “Applied elasticity,” *Longmans, Green and Co*, 1924.

[95] O.D. Kellogg, “Foundations of potential theory,” *New York: Murray Printng Company*, 1929.

[96] K.L. Johnson, “Contact mechanics,” *Cambridge: Cambridge University Press*, 1985.

[97] J. Canny, “A computational approach to edge detection,” *IEEE Transactions on Pattern Analysis and Machine Intelligence*, vol. PAMI-8, 1986, pp. 679-698.

[98] D. Xiao, H. Zhang, and M. Wirth, “Chemical modification of the surface of poly(dimethylsiloxane) by atom-transfer radical polymerization of acrylamide,” *Langmuir*, vol. 18, 2002, pp. 9971-9976.

[99] C. Gupta, G. A. Mensing, M. a Shannon, and P.J. A. Kenis, “Double transfer printing of small volumes of liquids,” *Langmuir : the ACS journal of surfaces and colloids*, vol. 23, 2007, pp. 2906-2914.

[100] H. Chen, Z. Zhang, Y. Chen, M.A. Brook, and H. Sheardown, “Protein repellant silicone surfaces by covalent immobilization of poly (ethylene oxide),” *Interface*, vol. 26, 2005, pp. 2391-2399.

[101] G. Elliott and A. Riddiford, “Dynamic contact angles I. The effect of impressed motion,” *Journal of colloid and interface science*, vol. 23, 1967, pp. 389-398.

[102] M.K. Chaudhury and G.M. Whitesides, “Direct measurement of interfacial interactions between semispherical lenses and flat sheets of poly(dimethylsiloxane) and their chemical derivatives,” *Langmuir*, vol. 7, 1991, pp. 1013-1025.

[103] P. Silberzan, S. Perutz, E.J. Kramer, and M.K. Chaudhury, “Study of the self-adhesion hysteresis of a siloxane elastomer using the JKR method,” *Langmuir*, vol. 10, 1994, pp. 2466-2470.

[104] A. Olah and G. Vancso, “Characterization of adhesion at solid surfaces: Development of an adhesion-testing device,” *European Polymer Journal*, vol. 41, 2005, pp. 2803-2823.

[105] E. Kroner, R. Maboudian, and E. Arzt, “Effect of repeated contact on adhesion measurements involving polydimethylsiloxane structural material,” *IOP Conference Series: Materials Science and Engineering*, vol. 5, 2009, pp. 012004.

[106] I. Lin, Y. Liao, Y. Liu, K. Chen, and X. Zhang, “Elastic and viscoelastic characterization of polydimethylsiloxane (PDMS) for cell-mechanics applications,” *Materials Research Society Symposium Proceedings*, 2008, pp. 81-86.

[107] A. Galliano, S. Bistac, and J. Schultz, “The role of free chains in adhesion and friction of poly(dimethylsiloxane) (PDMS) networks,” *The Journal of Adhesion*, vol. 79, 2003, pp. 973-991.

[108] A. Galliano, “Adhesion and friction of PDMS networks: molecular weight effects,” *Journal of Colloid and Interface Science*, vol. 265, 2003, pp. 372-379.